Available online at www.sciencedirect.com

ScienceDirect

Journal of Catalysis 246 (2007) 325–343

JOURNAL OF CATALYSIS

www.elsevier.com/locate/jcat

# Edge wetting effects of $\gamma$-$Al_2O_3$ and anatase-$TiO_2$ supports by $MoS_2$ and CoMoS active phases: A DFT study

D. Costa [a,b], C. Arrouvel [a], M. Breysse [b], H. Toulhoat [c], P. Raybaud [a,*]

[a] *Direction Chimie et Physico-Chimie Appliquées, Institut Français du Pétrole, 1-4 avenue de Bois-Préau, 92852 Rueil-Malmaison Cedex, France*
[b] *Laboratoire de Réactivité de Surface – UMR 7609 CNRS, Université Pierre et Marie Curie, 4 Place Jussieu, 75252 Paris Cedex 05, France*
[c] *Direction Scientifique, Institut Français du Pétrole, 1-4 avenue de Bois-Préau, 92852 Rueil-Malmaison Cedex, France*

Received 3 October 2006; revised 4 December 2006; accepted 6 December 2006

## Abstract

In the same spirit as a recent periodic DFT study on the interaction of $MoS_2$ layers on $\gamma$-alumina and anatase-$TiO_2$ surfaces [C. Arrouvel et al., J. Catal. 232 (2005) 161], the present DFT investigation brings new insights comparing the thermodynamic stability of $MoS_2$ particles anchored by S-edge and Mo-edge on these two supports under HDS conditions. It is shown that the S-edge interacts more weakly with the $\gamma$-alumina and anatase-$TiO_2$ surfaces. In particular, the epitaxial relationship found for the Mo-edge is not recovered for the S-edge on anatase. The determination of adhesion energies of $Mo_5CoS_n$ clusters on the two supports shows that Co weakens the edge anchoring of the active phase. The equilibrium morphology and the edge-wetting regime of the supported $MoS_2$ particles are deduced using the Gibbs–Curie–Wulff formalism. The DFT results combined with the morphological models of supported particles lead to a precise evaluation of the proportion of anchored and free edge sites (including the relative distribution of S-edge and Mo-edge sites). This analysis provides a new interpretation based on the edge-wetting concept of the two supports by $MoS_2$ and CoMoS particles to explain the different HDS activities observed.

*Keywords:* Anatase-$TiO_2$; $\gamma$-Alumina ($\gamma$-$Al_2O_3$); $MoS_2$; CoMoS–NiMoS; Hydrodesulfurization (HDS) catalysts; Density functional theory (DFT); Wetting effects; Surface; Epitaxy

## 1. Introduction

The price incentive of processing ever heavier petroleum crude oils, together with the continuous strengthening of environmental constraints, imply that meeting specific targets for ultra-low-sulfur diesel remains a real challenge. Research efforts are still needed to understand different aspects of the industrial hydrodesulfurization (HDS) catalysts composed of $\gamma$-alumina supported Co(Ni)MoS [1,2]. Among these components, the active phase–support interaction may play a key role in the resulting activity and selectivity. Changing the phase of the oxide support implies significant changes to the HDS activity. Two interesting reviews have highlighted these experimental results in detail [3,4] and pointed out that comparing $\gamma$-alumina with other supports, such as anatase-$TiO_2$, raises key questions in the exploration of the influence of the support on HDS catalysis. In particular, it is observed that the thiophene HDS activity (normalized by Mo atoms) is higher on anatase-$TiO_2$ support than on $\gamma$-alumina [5,6]. Even if numerous proposals were put forward to explain these observations, such as electronic effects [5], orientation effects [7], or indirect promotion by Ti [8–10], the interpretation remains open, particularly as far as promoter effects are concerned. Indeed, for the same Mo loading, the HDS activity of thiophene is promoted by Co by a factor of 7.6 on alumina but by only a factor of 3.3 on anatase [5]. Other authors have reported even higher activity for CoMo and NiMo/$Al_2O_3$ than for CoMo and NiMo/$TiO_2$ [6,11,12]. Therefore, the investigation of the active phase–support interface at an atomistic level is of paramount importance for making new progress in understanding the effects of the support, including active phase dispersion, electronic effects, and orientation effects.

---

[*] Corresponding author. Fax: +33 1 47 52 70 58.
*E-mail address:* pascal.raybaud@ifp.fr (P. Raybaud).

0021-9517/$ – see front matter © 2006 Elsevier Inc. All rights reserved.
doi:10.1016/j.jcat.2006.12.007

As highlighted in a recent review [13], first-principles calculations have made significant progress in the characterization of the structural, electronic and reactive properties of the Co(Ni)MoS active phase. Such studies have addressed key questions, including the localization of the Co(Ni) promoters [14,15], their role in modifying active nanoparticle morphologies [16], and active site reactivity [17]. More recently, preliminary investigations of the relevant surfaces of $\gamma$-alumina [18–20] and anatase-$TiO_2$ [21,22] and their interaction with $MoS_2$ clusters [23] under HDS conditions have been considered. It must be stressed that even if EXAFS data have provided some insight into the local distances and coordination at the interface between the active phase and the support [24], extracting an atomistic representation of the active phase–support interface remains a very difficult task. Consequently, modern first-principles techniques appear particularly well suited for furnishing improved concepts at the active phase–support interface.

The previous study [23] focusing on the DFT study of the $MoS_2$–support interaction, considering two supports, $\gamma$-alumina and anatase-$TiO_2$, aimed at gaining new insights into the role of active phase–support interaction in the resulting HDS activity for nonpromoted system. Particular attention had been devoted to the realistic representation of the support; it involved a nonspinel model for the $\gamma$-alumina bulk, resulting from the topotactic transformation of boehmite into $\gamma$-alumina [25] and the relevant surfaces with hydroxyl and sulfur species, which are stable under HDS conditions [18,19,22]. The same approach was performed for anatase [21,22,26]. For both supports, different surface orientations were considered to account for the morphology of the individual support nanocrystallites. It is also important to recall that only the interaction of $Mo_6S_n$ clusters representing the Mo-edge termination of $MoS_2$ nanoparticles with the supports was investigated previously [23]. Various possible types of interactions were considered, involving either iono–covalent bonds (e.g., Mo–O–Al), which are susceptible to be formed when the particle is anchored through the edge or the corner to the support or H bonds and dispersive interactions, both of which may be responsible for the parallel orientation of single $MoS_2$ sheets.

In addition, an epitaxial relationship of the Mo-edge of $MoS_2$ with anatase (110) or (001) surfaces was found. When size effects are taken into account, particles up to 90 Å in diameter may be anchored through the Mo-edge on the anatase surface. Such a strong interaction is not evidenced for alumina. Only particles with Mo-edge length $<15$ Å are found to interact strongly with the support and particles of larger size parallel to the surface. From this epitaxial relationship, two factors may explain the increased catalytic activity of $MoS_2$/anatase versus $MoS_2$/alumina: the stabilization of small anchored particles (with a higher edge/surface ratio) and the existence of a stable S-vacancy at the edge of those anchored particles.

Previous studies showed that for isolated $MoS_2$ particles [27,28], the Mo-edge is energetically more stable than the S-edge termination over a wide range of chemical potentials, and thus under HDS conditions, the shape is a deformed hexagon with a predominant Mo-edge. For this reason, the Mo-edge termination was first chosen [23] to investigate the active phase–support interaction. However, the possibility that the S-edge termination also may be stabilized due to its specific interaction with the $\gamma$-alumina or anatase surfaces cannot be excluded. Hence, S-edge anchoring must be properly investigated. Recent DFT calculations by Hinnemann et al. [29] suggested the possible addition of OH species on the S-edge. Because OH species are produced from water molecules and not from the support surface, it is difficult to determine whether the S-edge can actually create bonds with the supports according to the latter study. Thus, further investigations at the interface of the S-edge coupled with a realistic model of the supports, are needed. Consequently, in the first part of the current work, the interaction of the S-edge with the two supports, $\gamma$-alumina and anatase, is studied, using the same approach and models for the surfaces as in previous work [23] according to HDS conditions.

The first objective of this paper is thus to gain complementary insights into the nonpromoted $MoS_2$ active phase–support interaction, with particular emphasis on the comparison between S-edge and Mo-edge orientation. In Section 3.1, we compare the isolated S-edge clusters with the Mo-edge clusters. In Sections 3.2 and 3.3, we cover the interaction of the nonpromoted S-edge clusters with four surfaces: $\gamma$-$Al_2O_3$ (100), (110) and $TiO_2$ (101), (001). As mentioned earlier, a significant challenge when considering the experimental catalytic results is to extend this approach to promoted systems that exhibit different behaviors with respect to the two supports. Thus, in Section 3.4 we consider the effect of the Co promoter on the active phase–support interaction using $CoMo_5S_n$ clusters. We extrapolate these results to larger particle sizes in Section 3.5, and propose an approach to solve the equilibrium morphology of the particles supported on $\gamma$-alumina and anatase in Section 3.6. Finally, we discuss the results with respect to the edge-wetting concept and in relation to available experimental data.

## 2. Methodology

Total energy calculations are performed using Density Functional Theory (DFT) and the generalized gradient approximation (GGA) approach of Perdew and Wang [30]. To solve the Kohn–Sham equations, we use the Vienna ab initio Simulation Package (VASP) [31]. The electronic convergence criterion is fixed at 0.1 meV per cell. The eigenstates of the electron wavefunctions are expanded on a plane waves basis set using pseudopotentials to describe the electron–ion interactions within the projector augmented waves (PAW) approach [32]. For all total energy calculations, we use a cutoff energy of 258.7 eV. According to the enlarged supercell sizes within the surface plane (with respect to [21]), Brillouin zone sampling can be reduced at the $\Gamma$-point only. In the direction perpendicular to the surface, the slab thickness is decreased to keep system sizes within reach of DFT calculations (up to 250 atoms per supercell). The geometric optimization is carried out by calculating the Hellmann–Feynman forces, with an energy convergence criterion of 1 meV.

In the same spirit as for our previous study of the interaction between $Mo_6S_n$ clusters with Mo-edge and the support surfaces [23], the thermodynamic model based on the relative chemical potential of sulfur, $\Delta\mu_S$, as the main thermodynamic variable, was used to include gas-phase conditions ($p_{H_2}$, $p_{H_2S}$, and $T$). The values of $\Delta\mu_S$ as functions of $T$ and $p_{H_2S}/p_{H_2}$ are given by the diagram given in supplementary materials to help the reader to convert $\Delta\mu_S$ (used in the text) to the reaction conditions. For the current study, the $MoS_2$ active phase is represented by triangular $Mo_6S_n$ clusters exposing S-edges with various S-coverages similar to those described previously [27]. The isolated $Mo_6S_n$ clusters are described in Section 3.1; the $CoMo_5S_n$, in Section 3.6. The slab models representing the support surfaces exhibit the stable hydroxylation and sulfidation states determined in our earlier study [21]. In the present work, the reaction conditions correspond to a temperature range of 600–700 K and a water partial pressure of 0.01 bar. This implies that the chemical species at the supports surface is kept unchanged for the range of $H_2S$ and $H_2$ partial pressures investigated.

The adhesion energy of the $Co_xMo_6S_n$ clusters (with $x = 0$ or 1) on the $(hkl)$ surface of the support is defined by:

$$E_{adh/hkl} = E_{Co_xMo_{6-x}S_n/hkl} - E_{hkl} - E_{Co_xMo_{6-x}S_n}, \tag{1}$$

where $E_{Co_xMo_{6-x}S_n/hkl}$ represents the total energy of the $Co_xMo_6S_n$ cluster adsorbed on the $(hkl)$ surface, is the total energy of the $(hkl)$ surface, $E_{Co_xMo_{6-x}S_n}$ and the reference energy of the isolated $Co_xMo_6S_n$ cluster. The adsorption energy is negative for an exothermic process.

The geometry of the $Co_xMo_{6-x}S_n$ clusters and of the two outermost atomic layers of the supports are optimized. Because the cluster is adsorbed on one side of the slab, corrections for dipole–dipole interactions are included.

As described in detail previously [23], the Gibbs free energy of the nonpromoted $Mo_6S_n$ cluster adsorbed on the support $(hkl)$ surface is given by the following relationships, when expressed with respect to the bulk $MoS_2$ phase:

$$\Delta G_{Mo_6S_n/hkl} = \Delta G_{MoS_2} + \varGamma_{Mo_6S_n/hkl}, \tag{2}$$

where

$$\varGamma_{Mo_6S_n/hkl} = \varGamma_{Mo_6S_n} + \frac{1}{6}E_{adh/hkl} \tag{3}$$

and

$$\varGamma_{Mo_6S_n} = \varGamma_0(Mo_6S_n) - \frac{n-12}{6}\Delta\mu_S. \tag{4}$$

Here $\Delta G_{MoS_2}$ represents the Gibbs free energy of the $MoS_2$ bulk phase (about $-2.76$ eV/Mo). $\varGamma_{Mo_6S_n}$ represents the energy required to create the Mo-edges of the isolated cluster, whereas $\varGamma_0$ is the energy required to create the edges at $\Delta\mu_S = 0$ (both are positive values and expressed in eV per Mo-edge atom). $\varGamma_{Mo_6S_n/hkl}$ is the surface energy of the supported cluster. The lowest $\varGamma_{Mo_6S_n/hkl}$ values determine the stable adsorption configurations of the $Mo_6S_n$ clusters as a function of the sulforeductive conditions. To determine $E_{adh/hkl}$, numerous configurations for the adsorbed clusters have been tested. The parallel orientation involves H bonds and/or weak electrostatic interactions between the $Mo_6S_n$ basal plane and the support. Different types of perpendicular orientations (through one S-edge, corner, basal plane) were considered.

For the promoted CoMoS systems, our investigation is based on the analysis of the variation of the adhesion energy [Eq. (1)] after the addition of promoter. In particular, a systematic analysis of stoichiometries and corresponding $\Delta G_{Co_xMo_{6-x}S_n/hkl}$ as a function of the chemical potential is beyond the scope of the present work.

For large clusters, as explained previously [23], we use an approach for extrapolating our DFT results by simultaneously accounting for long-range interactions between correlated charge fluctuations, which are underestimated in the DFT formalism. In particular, the van der Waals interactions between the basal S-atom layer in the $MoS_2$ systems and the O-atom network of the supports are expected to modify the energies for large particle sizes. Because it is not yet possible to carry out a self-consistent treatment of the van der Waals contributions in DFT, we use force-field approaches to estimate the long-range effects and add van der Waals contributions in the adhesion energy term. According to [23], the van der Waals contributions are thus expected to be less than 10 kJ/mol of basal S atoms and depend slightly on the type of oxide surface. This estimate seems reasonable when compared with the van der Waals binding energy of the $MoS_2$ layers found within the fully nonlocal functional formalism recently proposed by Rydberg et al. [33]. The extrapolation formulas used for the S-edge interaction are given in supplementary materials.

In addition, we carried out a morphology analysis based on the Gibbs–Curie–Wulff–Kaischew equations. For the sake of clarity, the details of this approach are reported in Section 3.6.

## 3. Results

### 3.1. Isolated $Mo_6S_n$ clusters with S-edge

To model the interaction between the active phase and the support, small triangular $Mo_6S_n$ clusters exhibiting three S-edges with different S coverages (i.e., S vacancies) were used, in a similar manner as performed previously for the Mo-edge clusters [23]. From the fully sulfided cluster $Mo_6S_{20}$ (Fig. 1a), covered with 100% S, sulfur atoms are gradually removed to create S vacancies at either the corner (c) or the edge (e), leading to a S coverage of 50% S at the edge and gradually to a 0% S edge. The S-depopulated edge interacts with the support surface. For a given stoichiometry, there are several possible choices for the removal of S atoms. In contrast to the previous study, only the cluster's edge anchored to the support was gradually depopulated by S atoms; indeed, the removal of S atoms on the three edges simultaneously led to highly unstable S-deficient structures not relevant for HDS conditions. The two remaining edges were kept at 100% S, as shown in Fig. 1. The nonequivalent edge's stoichiometry is included in Eq. (4) to consistently determine the $\Delta G$ diagram as a function of the chemical potential of S.

Fig. 1 shows the optimized structures of the isolated $Mo_6S_n$ clusters. For sake of consistency, the notations as explained in

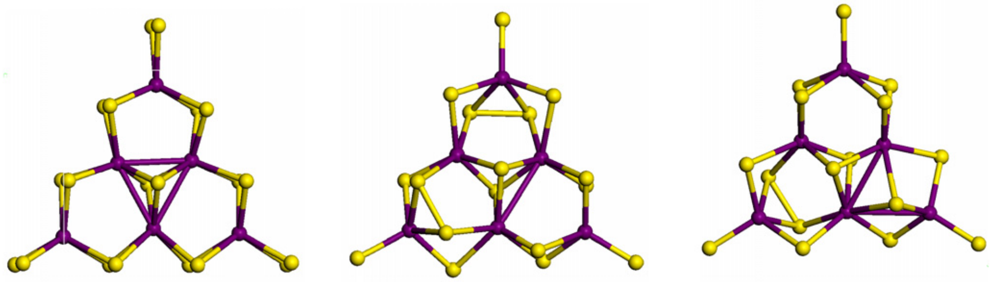

(a) $Mo_6S_{20}$ (100% S) (b) $Mo_6S_{17}$ (100% S, 3c) (c) $Mo_6S_{16}$ (100% S, 3c, 1e)

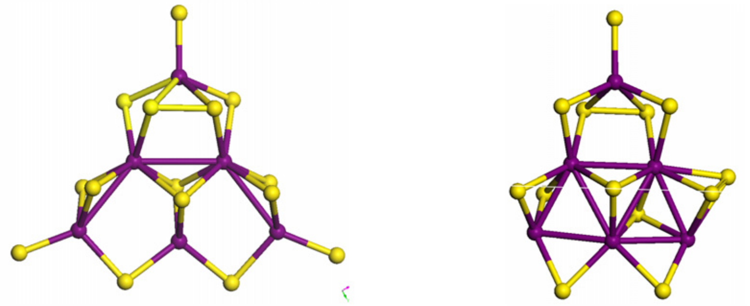

(d) $Mo_6S_{15}$ (50% S, 3c) (e) $Mo_6S_{13}$ (50% S, 5c)

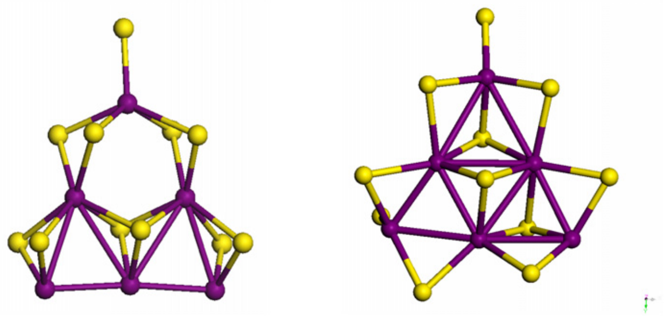

(f) $Mo_6S_{11}$ (0% S, 5c) ⟶ (g) $Mo_6S_{11}$ (0% S, 5c)

Fig. 1. Stoichiometry, optimized structure and notations for the different $Mo_6S_n$ clusters (violet balls, molybdenum atoms; yellow balls, sulfur atoms). (100% S, 3c) means 100% S coverage at the edge with three corner vacancies. (For interpretation of the references to color in this figure legend, the reader is referred to the web version of this article.)

the figure are similar to those of our previous study [23]; the clusters are as follows:

- The $Mo_6S_{20}$ cluster (Fig. 1a), a model for the 100% S at the edges, with no sulfur vacancy.
- The $Mo_6S_{17}$ cluster (Fig. 1b), exhibiting one S vacancy at each corner, with a S-coverage of 100% at the edges.
- The $Mo_6S_{16}$ cluster (100% S, 3c, 1e, Fig. 1c), exhibiting three corner vacancies and one edge vacancy. For this cluster, the creation of two S vacancies at one corner (100% S, 4c [not shown]) allows the study of the interaction of a totally depopulated corner with the support surfaces.
- The $Mo_6S_{15}$ (resp. $Mo_6S_{13}$) (Figs. 1d and 1e) cluster, containing one 50% S-covered edge and two other edges covered with 100% S. $Mo_6S_{15}$ has one S vacancy at each corner, whereas $Mo_6S_{13}$ has two corners with two S-vacancies and one S-vacancy.
- The nonreconstructed metastable $Mo_6S_{11}$ cluster, exposing 0% S on one edge, with two sulfur vacancies at each corner terminating this edge (Fig. 1f). This configuration has a high Gibbs free energy resulting from a strong reconstruction and leading to the deformed structure shown in Fig. 1g. The Gibbs free energy for $\Delta\mu_S = 0$ of this distorted cluster (Table 1) is significantly reduced, by about 1.12 eV, with respect to the nonreconstructed one. Such a reconstruction can be observed only on such a small and isolated cluster. A similar result was previously reported for the Mo-edge cluster with $Mo_6S_{11}$ composition [23]. In the same way, the nonreconstructed $Mo_6S_{11}$ (0% S, 3c of Fig. 1f) is considered to study the interaction of a 0% S edge with the support.

Table 1
Gibbs free energy (in eV per Mo atom at the S-edge) of the isolated $Mo_6S_n$ clusters in several configurations and adhesion energies (in eV per cluster) as a function of the orientation (∥, ⊥, tilted) on the $Al_2O_3$ (100) and (110) surfaces and on the $TiO_2$ (100) and (101) surfaces

| $Mo_6S_n$ | $n-12$ | $\Gamma_0$ | Orientation | $\gamma$-Alumina | | Anatase-$TiO_2$ | |
|---|---|---|---|---|---|---|---|
| (S-coverage) | | | | $E_{adh/100}$ | $E_{adh/110}$ | $E_{adh/101}$ | $E_{adh/001}$ |
| $Mo_6S_{20}$ (100% S) | 8 | 1.14 | Parallel ∥ | −0.16 | −0.24 | −0.01 | −0.14 |
| $Mo_6S_{17}$ (100% S, 3c) | 5 | 1.26 | Parallel ∥ | −0.13 | −0.34 | −0.15 | −0.30 |
| $Mo_6S_{16}$ (100% S, 3c, 1e) | 4 | 1.31 | Parallel ∥ | −0.06 | −0.30 | −0.15 | −0.19 |
| $Mo_6S_{16}$ (100% S, 2c, 2e) | 4 | 1.34 | Tilted | −0.15 | +0.14 | −0.12 | +0.93 |
| | | | | −0.02 | +0.27 | +0.01 | +1.06 |
| $Mo_6S_{16}$ (100% S, 3c, 1e) | 4 | 1.46 | Ortho ⊥ | −0.57 | −1.48 | −0.89 | −1.19 |
| | | | | +0.32 | −0.59 | +0.01 | −0.30 |
| $Mo_6S_{15}$ (50% S, 3c) | 3 | 1.66 | Parallel ∥ | −0.29 | −0.25 | −0.12 | −0.16 |
| | | | Tilted | −0.37 | −0.23 | −0.37 | +1.31 |
| | | | Ortho ⊥ | +1.25 | +0.59 | +1.40 | +0.97 |
| $Mo_6S_{13}$ (50% S, 5c) | 1 | 1.84 | Parallel ∥ | −0.04 | −0.04 | −0.09 | −0.37 |
| | | | Tilted | −0.60 | −1.27 | −0.03 | −0.15 |
| | | | Ortho ⊥ | +1.73 | +1.79 | +0.85 | −1.50 |
| $Mo_6S_{11}$ (50% S, 3c) | −1 | 1.85 | Ortho ⊥ | +4.72 | +2.16 | +1.66 | +0.48 |

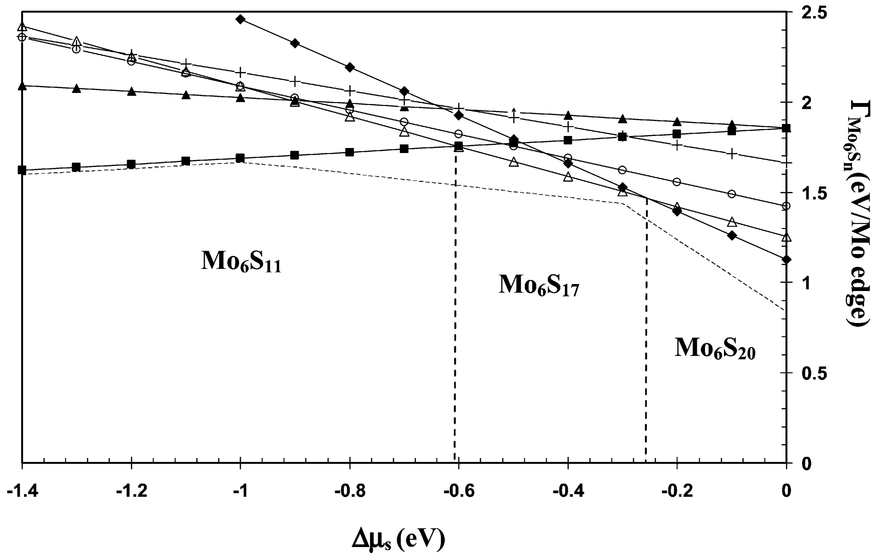

Fig. 2. Gibbs free energy of the isolated S-edge $Mo_6S_n$ clusters and comparison with the Mo-edge clusters: (◆) $Mo_6S_{20}$ (100% S); (△) $Mo_6S_{17}$ (100% S, 3c); (○) $Mo_6S_{16}$ (100% S, 3c, e), (+) $Mo_6S_{15}$ (50% S, 3c); (▲) $Mo_6S_{13}$ (50% S, 5c); (■) $Mo_6S_{11}$ (50% S, 5c); the most stable stoichiometry of the S-edge clusters is also indicated as a function of $\Delta\mu_S$. The envelop of the minima Mo-edge clusters surface energies (from [23]) is represented in dotted lines.

Fig. 2 shows the Gibbs energy diagram of the isolated S-edge clusters as the function of the chemical potential of sulfur. At a given chemical potential of sulfur, the lower the Gibbs free energy, the more stable the corresponding stoichiometry. As already observed for large Mo-edge clusters [16], in a sulfiding atmosphere, the fully sulfided edge ($Mo_6S_{20}$) is favored, whereas clusters with 50% S at the edge and eventually an S vacancy at the corner are stabilized at low $H_2S$ partial pressure, including HDS conditions ($-1 < \Delta\mu_S < -0.8$ eV).

To compare the stability diagrams of the Mo-edge and S-edge $Mo_6S_n$ clusters, Fig. 2 also shows the Gibbs free energies of the most stable configurations of the Mo-edge $Mo_6S_n$ clusters found previously [23]. Under sulfiding conditions (i.e., high $\Delta\mu_S$), the Mo-edge is significantly more stable than the S-edge; in contrast, under more reducing conditions (i.e., lower $\Delta\mu_S$), the free energies of the Mo-edge and S-edge become closer, consistent with previous results obtained for larger cluster sizes [27] and observed experimentally by STM [34]. However, for these small-sized clusters, the difference between the S-edge energy and Mo-edge energy appears to be less pronounced. Moreover, the $Mo_6S_{11}$ cluster with 0% S is stabilized after relaxation in a wider range of chemical potentials on the S-edge ($\Delta\mu_S < -0.65$ eV). We note that this reconstructed cluster has a structure and an energy very similar to those of the Mo-edge cluster.

### 3.2. $Mo_6S_n$ clusters supported on $\gamma$-$Al_2O_3$

#### 3.2.1. $\gamma$-$Al_2O_3$ (100) surface

This surface is not hydroxylated under HDS conditions [21], and the surface Al and oxygen atoms do not exhibit a high degree of nonsaturation ($Al_V$ and $\mu_3$-O) with respect to the bulk ($Al_{IV}$, $Al_{VI}$, and $\mu_3$-O). This rather rigid surface is not very reactive, and the adhesion energies are weak (Table 1). As in our

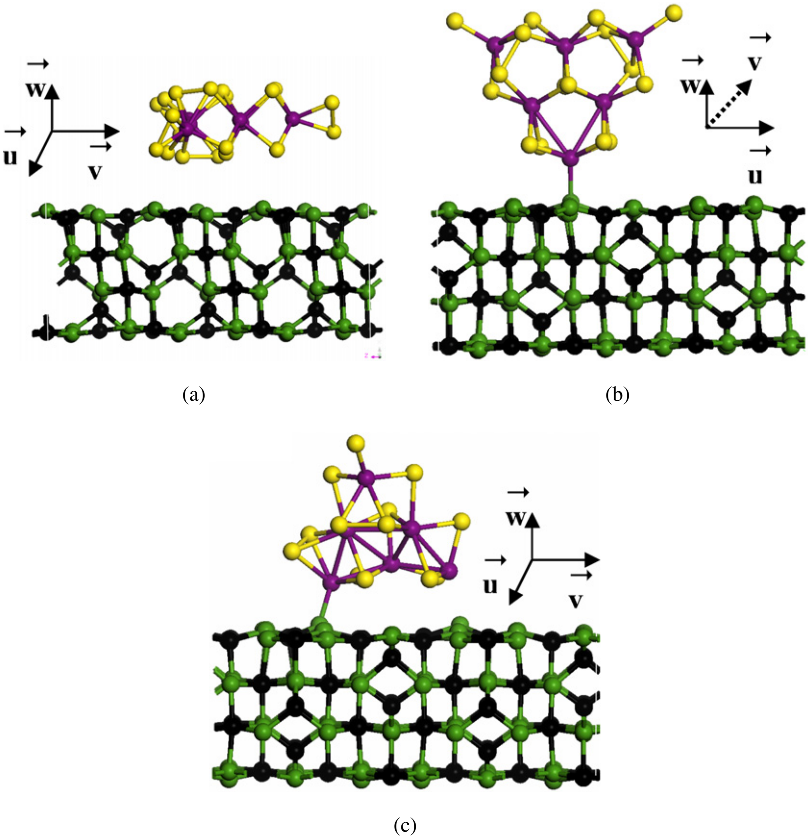

Fig. 3. Optimized structures of (a) $Mo_6S_{20}$ (100% S, ‖); (b) $Mo_6S_{16}$ (100% S, 4c, ⊥); (c) $Mo_6S_{13}$ (50% S, 5c, tilted) adsorbed on $\gamma$-$Al_2O_3$ (100) surface. For the alumina slab: black balls, aluminum atoms; green balls, oxygen. For the $Mo_6S_n$ clusters: violet balls, molybdenum atoms; yellow balls, sulfur atoms. (For interpretation of the references to color in this figure legend, the reader is referred to the web version of this article.)

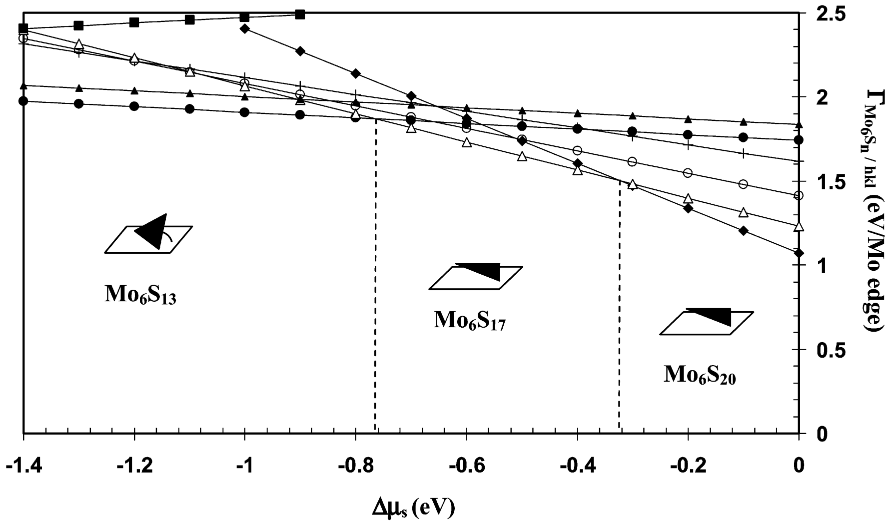

Fig. 4. Gibbs free energy of the clusters adsorbed on the $\gamma$-$Al_2O_3$ (100) surface: (◆) $Mo_6S_{20}$ (100% S, ‖); (△) $Mo_6S_{17}$ (100% S, 3c, ‖); (○) $Mo_6S_{16}$ (100% S, 3c, e, ‖); (+) $Mo_6S_{15}$ (50% S, 3c, ‖ or tilted); (▲) $Mo_6S_{13}$ (50% S, 5c, ‖); (●) $Mo_6S_{13}$ (50% S, 5c, tilted); (■) $Mo_6S_{11}$ (0% S, 5c, ⊥).

previous work, here we considered three types of interaction: parallel, orthogonal, and tilted. Fig. 3 shows the relevant types of adsorption modes for the different cluster stoichiometries on the $\gamma$-alumina (100) surface. Fig. 4 shows the Gibbs free energy diagrams of the same clusters adsorbed in different configurations on the alumina (100) surface, including the chemical potential of sulfur. The clusters $Mo_6S_{20}$ and $Mo_6S_{17}$ lie parallel to the surface and are stable for $-0.76 < \Delta\mu_S < 0$ eV. Fig. 3a shows the corresponding configuration for the $Mo_6S_{20}$ cluster; a similar configuration is obtained for $Mo_6S_{17}$. Fig. 3b shows the perpendicular configuration anchored through a single point on the corner for the $Mo_6S_{16}$ cluster, which is less stable than the parallel configuration. The $Mo_6S_{13}$ (50% S, 5c) cluster is stabilized for $\Delta\mu_S < -0.76$ eV in a tilted configura-

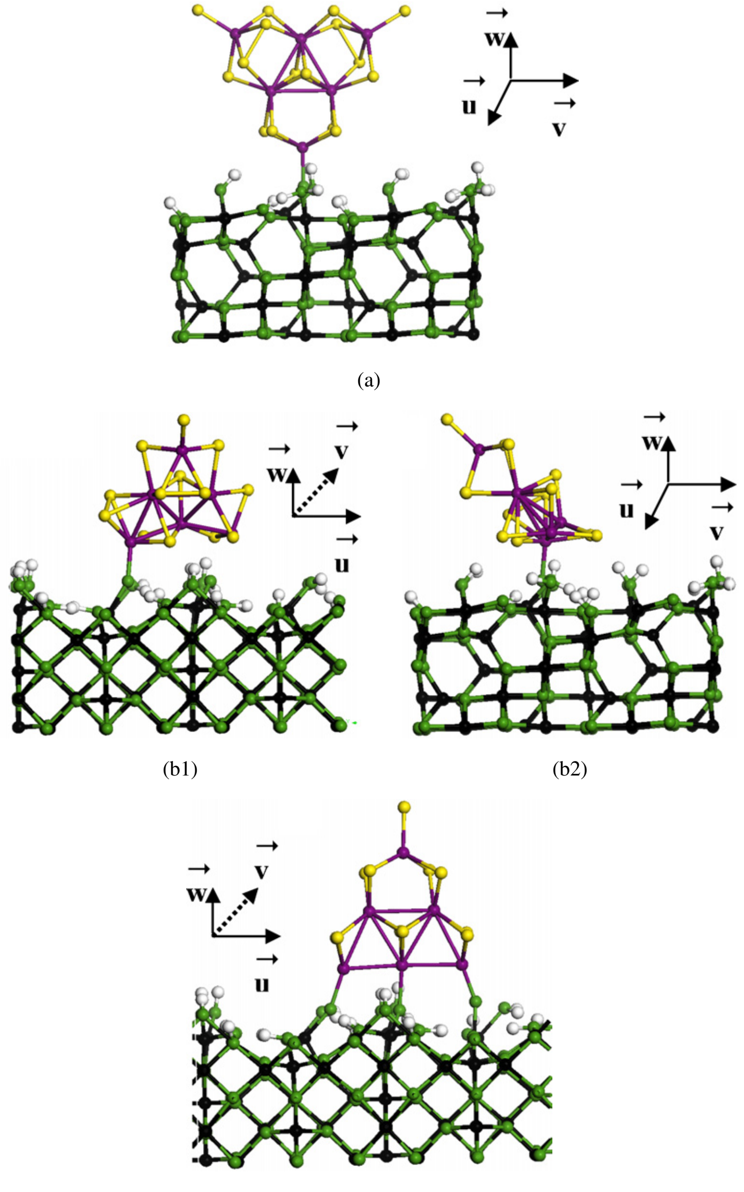

(a)

(b1) (b2)

(c)

Fig. 5. Optimized structures of (a) $Mo_6S_{16}$ (100% S, 4c, ⊥); (b1) and (b2) front and side views of $Mo_6S_{13}$ (50% S, 5c, tilted); (c) $Mo_6S_{11}$ (0% S, 5c, ⊥) adsorbed on $\gamma$-$Al_2O_3$ (110) surface. For the alumina slab: black balls, aluminum atoms; green balls, oxygen; white balls, hydrogen atoms. For the $Mo_6S_n$ clusters: violet balls, molybdenum atoms; yellow balls, sulfur atoms. (For interpretation of the references to color in this figure legend, the reader is referred to the web version of this article.)

tion with anchoring through one single Mo–O–Al bond at the corner (Fig. 3c). The local structural constraints of this configuration inhibit the formation of one or multiple Mo–O–Al–S–Mo rings; the next Mo atom binds solely to one O atom of the surface. A similar result was found for the Mo-edge. This implies that S-edge and Mo-edge anchoring are not favored on this surface.

### 3.2.2. *$\gamma$-$Al_2O_3$ (110) surface*

This surface is hydroxylated with 8.8 OH/$nm^2$ and is not sulfided [21]. Fig. 5 shows the different configurations obtained after geometry optimization, and Fig. 6 shows the corresponding Gibbs free energies diagram. For $-0.66 < \Delta\mu_S < 0$ eV, the clusters with high S-content lie parallel to the surface [not shown here for the sake of clarity, but similar to the configurations in Fig. 3a for the (100) surface]. For the $Mo_6S_{16}$ cluster, one Mo–O–Al bond is formed at the corner of the cluster (Fig. 5a); however, this bond is not stable on the surface. For $\Delta\mu_S < -0.66$ eV, there is a tilted anchoring through one Mo–O–Al bond of the $Mo_6S_{13}$, and the 50% S edge is stabilized with an adhesion energy of $-1.27$ eV (Table 1). For this cluster, anchoring through two Mo–O–Al bonds (not shown) was calculated to be less stable than the configuration shown in Fig. 5b, due to the mismatch between the Mo rows at the S-edge and the O network. In addition, no Mo–O–Al–S–Mo ring can be formed, but there is a flexible hydrogen bond between the S-atom of the $Mo_6S_{13}$ cluster and the hydroxyl group of the surface.

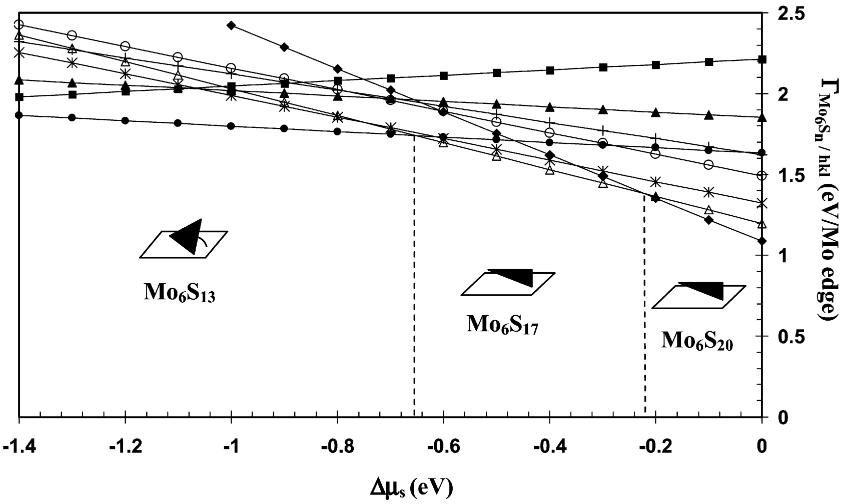

Fig. 6. Gibbs free energy of the clusters adsorbed on the $Al_2O_3$ (110) surface: (◆) $Mo_6S_{20}$ (100% S, ∥); (△) $Mo_6S_{17}$ (100% S, 3c, ∥); (✳) $Mo_6S_{16}$ (100% S, 4c, ⊥); (○) $Mo_6S_{16}$ (100% S, 3c, e, ∥); (+) $Mo_6S_{15}$ (50% S, 3c, ∥); (▲) $Mo_6S_{13}$ (50% S, 5c, ∥); (●) $Mo_6S_{13}$ (50% S, 5c, tilted); (■) $Mo_6S_{11}$ (0% S, 5c, ⊥).

The $Mo_6S_{11}$ cluster anchors through one S-edge fully depopulated from S atoms in a perpendicular orientation (Fig. 5c). The flexibility of $\mu_1$-Al–OH groups enhances the stability of Mo–O–Al bonds along one S-edge with respect to the (100) surface. This trend, already observed for the Mo-edge, is strengthened for the S-edge. However, this configuration is not stable when the chemical potential of sulfur is taken into account (Fig. 6).

### 3.3. $Mo_6S_n$ clusters supported on anatase-$TiO_2$

#### 3.3.1. Anatase (101) surface

Under HDS conditions, the (101) surface of anatase is dehydrated and not sulfided [21]. In contrast to the Mo-edge clusters, for which the adhesion energies were the highest for this surface [23], the adhesion energies remain as small as for S-edge clusters on $\gamma$-$Al_2O_3$ (110). Figs. 7 and 8 show the optimized configurations and the Gibbs free energy diagram of the clusters adsorbed on the anatase (101) surface. Over a wide range of chemical potential ($>-0.92$ eV), the $Mo_6S_{17}$ and $Mo_6S_{20}$ clusters lie parallel to the surface. For $\Delta\mu_S < -0.92$ eV, a perpendicular $Mo_6S_{11}$ cluster is stabilized, thanks to the formation of Mo–O covalent bonds with lengths of 1.97–2.19 Å. The relaxed Mo–Mo distances (2.64 and 2.67 Å, respectively) are much shorter than those in the $MoS_2$ bulk. The O atoms of the $TiO_2$ surface replace the missing bridging S of the cluster, because the O–O distance (3.8 Å) on the surface is compatible with the S–S distance in a 50% S edge cluster (3.6–3.7 Å).

We investigate whether an epitaxial relationship could exist for the S-edge clusters (as depicted in Figs. 7b1 and 7b2). For these configurations, the cluster ($Mo_6S_{15}$, 50% S, 3c) forms three covalent bonds with the surface: two Mo–O bonds of 2.08 and 2.31 Å and one S–Ti bond of 2.44 Å. Only one distorted Mo–O–Ti–S–Mo ring is formed at the corner, and the four involved atoms are not coplanar. Significant distortions in the Mo–Mo distances explain the destabilization of this configuration. The development of an epitaxial relationship is thus too expensive in terms of the cluster reconstruction energy. Consequently, in contrast to the results obtained on the Mo-edge [23] there is no epitaxial relationship between the S-edge and the (101) surface.

#### 3.3.2. Anatase (001) surface

The (001) anatase is hydroxylated and partially sulfided, with a hydroxyl coverage of 3.46 $OH/nm^2$ and an S coverage of 1.73 $S/nm^2$ [21]. Fig. 9 shows the different stable conformations obtained for the $Mo_6S_n$ clusters, and Fig. 10 reports the Gibbs free energies as a function of $\Delta\mu_S$. Again, the adhesion energies are smaller than for the Mo-edge. For $-0.3 < \Delta\mu_S < 0$ eV, the $Mo_6S_{20}$ cluster lies parallel to the surface. For $\Delta\mu_S < -0.3$ eV, a single point anchoring through one corner (Mo–S bond length 2.30 Å) is stabilized for the $Mo_6S_{13}$ (50% S, 5c) cluster, with the filling of one corner sulfur vacancy by the S atom belonging to the support's surface, and two additional H bonds between OH groups and S atoms of the cluster.

We have also checked for a possible epitaxial relationship. The $Mo_6S_{13}$ cluster might exhibit a tilted configuration, implying the formation of two Mo–O–Ti covalent bonds and two H bonds between OH groups and S atoms of the edge (Fig. 9b). As for the hydroxylated $\gamma$-$Al_2O_3$ (110) surface, a Ti–O–Mo–S···H–O–Ti ring is formed, inducing the cluster to tilt. However, as the Mo–Mo distances are shortened to 2.8 Å, the strong constraints at the interface lead to high energy for such a configuration. A multipoint anchoring was also simulated for the $Mo_6S_{11}$ (0% S) cluster, with the formation of two Ti–O–Mo–O rings separated by one Ti–S–Mo bond (as depicted in Fig. 9c). In contrast to the (100) surface, more than one Mo–S···H–O–Ti ring can be formed, due to the flexibility of the OH groups. The additional covalent bond formed with an S atom adsorbed on the surface, allows the filling of an S vacancy at the edge. However, this type of configuration cannot be stabilized due to the cost of deformation energy of the cluster. This implies that S-edge anchoring is not stable when the chemical potential of sulfur is included (Fig. 10). This result is in contrast with the findings for the Mo-edge, where anchoring along this edge was

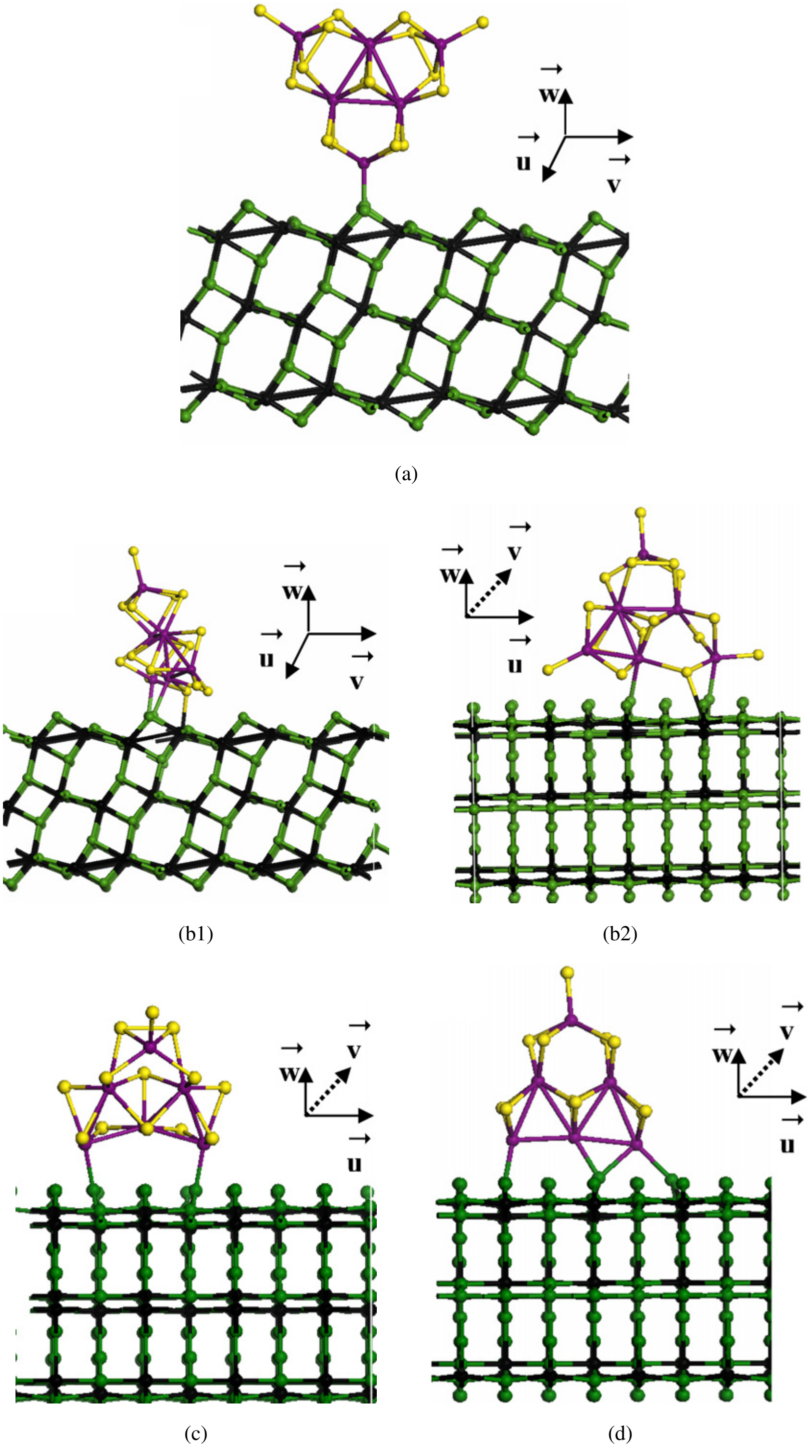

(a)

(b1)

(b2)

(c)

(d)

Fig. 7. Optimized structures of (a) $Mo_6S_{16}$ (100% S, 3c, e, $\perp$); (b1) and (b2) front and side views of the $Mo_6S_{15}$ tilted (50% S, 3c, tilted); (c) $Mo_6S_{13}$ (50% S, 5c, tilted); (d) $Mo_6S_{11}$ (0% S, 5c, $\perp$) adsorbed on $TiO_2$ (101) surface. For the titania slab: black balls, aluminum atoms; green balls, oxygen. For the $Mo_6S_n$ clusters: violet balls, molybdenum atoms; yellow balls, sulfur atoms. (For interpretation of the references to color in this figure legend, the reader is referred to the web version of this article.)

stabilized by the epitaxial relationship, as detailed in supplementary materials.

### 3.4. Co-promoted clusters

Previous DFT studies of isolated Co-promoted clusters [16] and periodic models [14,35] found a stable structural environment for Co atoms at the edges in the CoMoS phase. Under HDS conditions, Co is located in substitution for Mo at the edges with a preferential affinity for the S-edge [16]. In this section, we investigate how the presence of Co may modify the cluster's anchoring on the support. Investigating all possible stoichiometries of the $CoMo_5S_n$ promoted clusters (as done in previous sections for the nonpromoted case) is beyond the

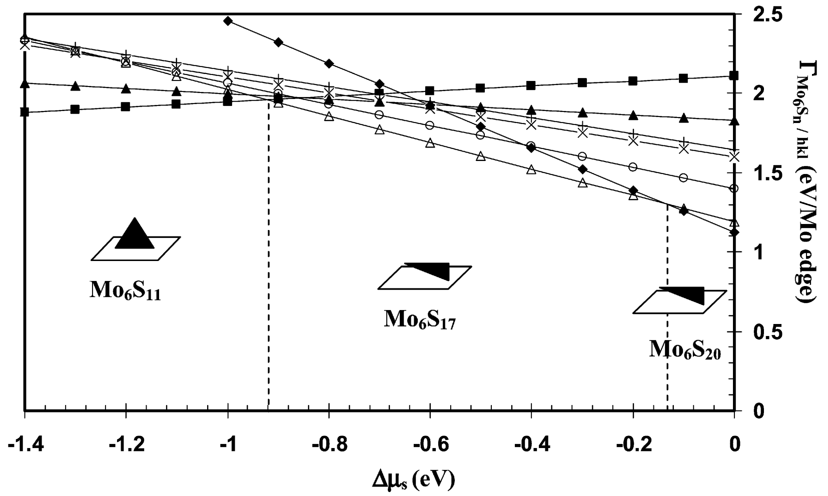

Fig. 8. Gibbs free energy diagram of the $Mo_6S_n$ clusters adsorbed on the anatase (101) surface. (◆) $Mo_6S_{20}$ (100% S, ‖); (△) $Mo_6S_{17}$ (100% S, 3c, ‖); (○) $Mo_6S_{16}$ (100% S, 3c, e, ‖); (+) $Mo_6S_{15}$ (50% S, 3c, ‖); (×) $Mo_6S_{15}$ (50% S, 3c, tilted); (▲) $Mo_6S_{13}$ (50% S, 5c, ‖ or tilted); (■) $Mo_6S_{11}$ (0% S, 5c, ⊥).

scope of the current study; therefore, we have chosen the most relevant configurations found for the nonpromoted clusters, and we analyze the impact of Co substitution at the edges or corners on the structures and energies.

Table 2 reports the adhesion energies of the Co-promoted clusters in comparison with the nondecorated ones for the four support surfaces. On the alumina (110) surface, the adsorption through Co at the corner (Fig. 11a) is less favorable than that through Mo. The optimized Co–O distance is 2.00 Å, smaller than the corresponding Mo–O distance (2.26 Å) found for the stable nonpromoted cluster [23]. The interaction of a promoted cluster anchored through the S-edge (Fig. 11b) is also less favorable. Although one Mo–O–Al bond is conserved at the corner, no Co–O–Al bond is formed, and the resulting adhesion energy is weak. On the alumina (100) surface, the adhesion energies decrease when the Mo-edge cluster is bound to the surface through the Co atom at the corner with a Co–O distance of 2.14 Å, slightly longer than on alumina (110). (Note that the Mo–O distance is 2.15 Å for the corresponding nonpromoted cluster [23].) No interaction of the promoted S-edge with the alumina (100) surface has been simulated. Indeed, it was previously found that on this face, the nonpromoted S-edge clusters are not chemically bonded with the surface (Table 1). Then, following a bond order conservation principle, it can be reasonably admitted that the strong stabilization of Co on the S-edge [16,36] prevents strong interaction between Co on the S-edge and the alumina surface. Consequently, Co atoms weaken the interaction by edges or corners on the $\gamma$-alumina support.

On the anatase (101) and (001) surfaces, all adhesion energies of the promoted cluster are reduced when Co is located at the edge. Formation of the Co–O bond destabilizes the epitaxial relationship observed for nonpromoted cluster. In Figs. 11c and 11d, the respective C–O lengths are 1.95 and 2.03 Å. For the corresponding nonpromoted cluster in epitaxy, the Mo–O distances are slightly longer, between 1.98 and 2.10 Å on anatase (101) and between 2.11 and 2.30 Å on anatase (001). However, the electronic effect of Co is to decrease the adhesion energy due to the smaller intrinsic Co–O bond energy with respect to Mo–O. In particular, for anatase (001), only one Co–O bond is found, whereas two Mo–O bonds are present for the corresponding nonpromoted cluster. Finally, the interaction of a promoted cluster is slightly increased on the (101) surface (with respect to the nonpromoted cluster) when Co is present at the corner (Fig. 11e), the resulting Co–O distance is 1.96 Å. In summary the presence of Co at the Mo-edge/support interface is not energetically favored with respect to an edge interaction involving Mo atoms preferentially.

### 3.5. Extrapolation for large particles

As in our previous work concerning Mo-edge clusters, we use a simplified approach to extrapolate the Gibbs free energies of triangular S-edge particles obtained in previous sections for larger supported particles. We have thus considered surface energies for large clusters calculated by Schweiger et al. [27] and add adhesion energy per Mo atom as determined in earlier sections or in previous work [23]. With increasing cluster size, the van der Waals contributions and/or hydrogen interaction between the S atoms of the basal plane of the $MoS_2$ particle and oxygen or hydroxyls become predominant, thus stabilizing parallel configurations with respect to the tilted or orthogonal ones. The model used allows determination of Mo per edge ($k$), characterizing the size, and $k_T$, the threshold value corresponding to the transition from chemical interaction (perpendicular orientation) to predominant van der Waals or hydrogen-bonding interaction (parallel orientation).

For the anatase-$TiO_2$ (101) and $\gamma$-alumina (110) surfaces, Fig. 12 shows the variation of edge energy as a function of size for HDS conditions ($\Delta\mu_S = -0.9$ eV). On the anatase (101) surface, $k_T$ is significantly smaller for the S-edge ($k_T = 5$) than for the Mo-edge ($k_T = 14$), meaning that particles are anchored preferentially through the Mo-edge. Furthermore, the Mo-edge Gibbs free energy remains smaller than the S-edge energy, whatever the size may be. This important insight will play a role in the equilibrium morphologies of supported par-

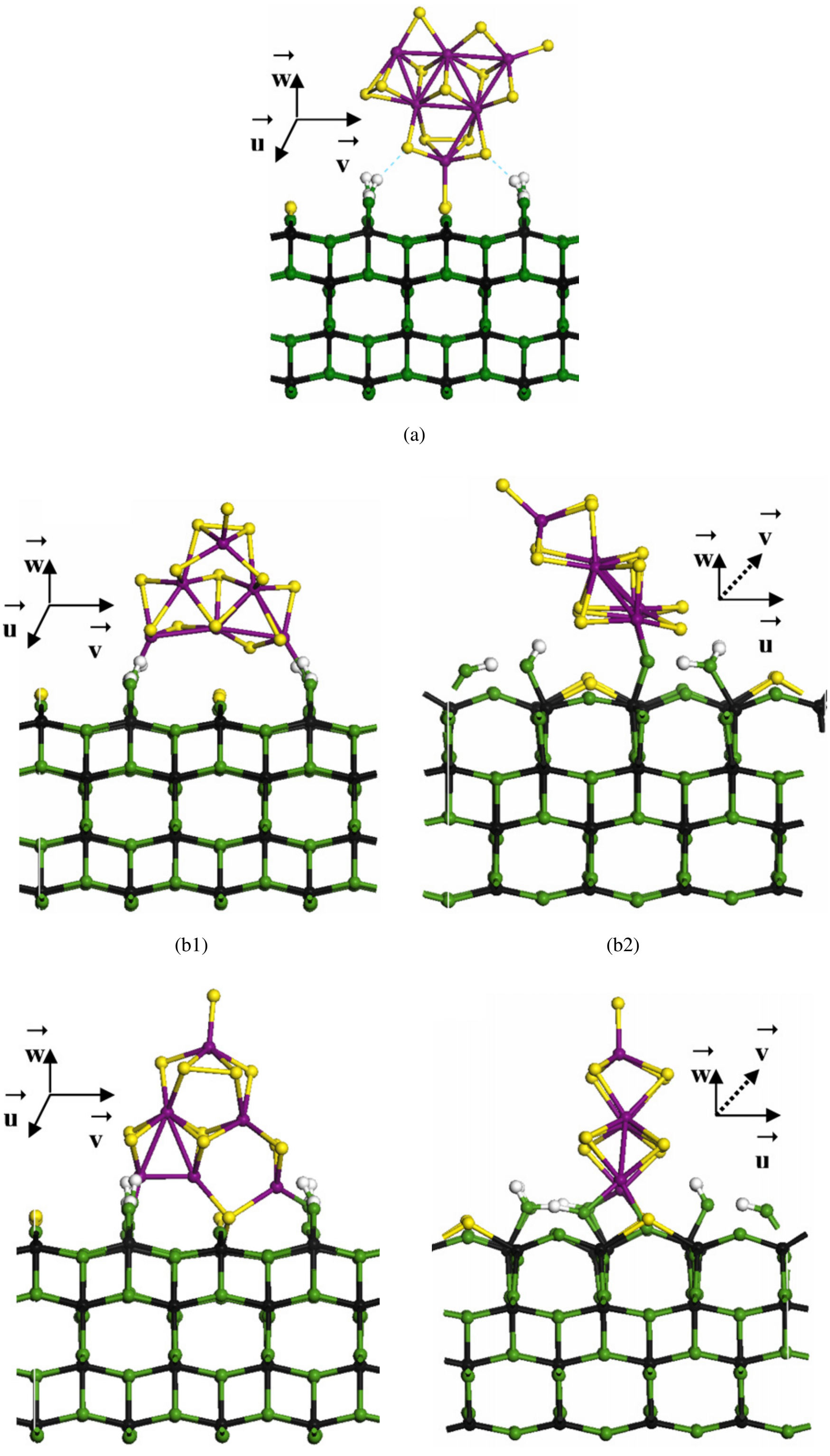

(a)

(b1) (b2)

(c1) (c2)

Fig. 9. Optimized structures of (a) $Mo_6S_{13}$ (50% S, 5c, ⊥); (b1) and (b2) front and side views of $Mo_6S_{13}$ (50% S, 5c, tilted); (c1) and (c2) front and side views of $Mo_6S_{11}$ (0% S, 5c, ⊥) adsorbed on $TiO_2$ (001) surface. For the titania slab: black balls, aluminum atoms; green balls, oxygen; white balls, hydrogen atoms. For the $Mo_6S_n$ clusters: violet balls, molybdenum atoms; yellow balls, sulfur atoms. (For interpretation of the references to color in this figure legend, the reader is referred to the web version of this article.)

ticles, as discussed in the next section. In contrast, for the $\gamma$-alumina (110) surface, the parallel orientation of both S-edge and Mo-edge clusters is the most stable in the whole range of chemical potential investigated, with $k_T$ values of 5. Due to edge anchoring, a significant decrease of the edge energy is observed on anatase. Table 3 also reports the numerical val-

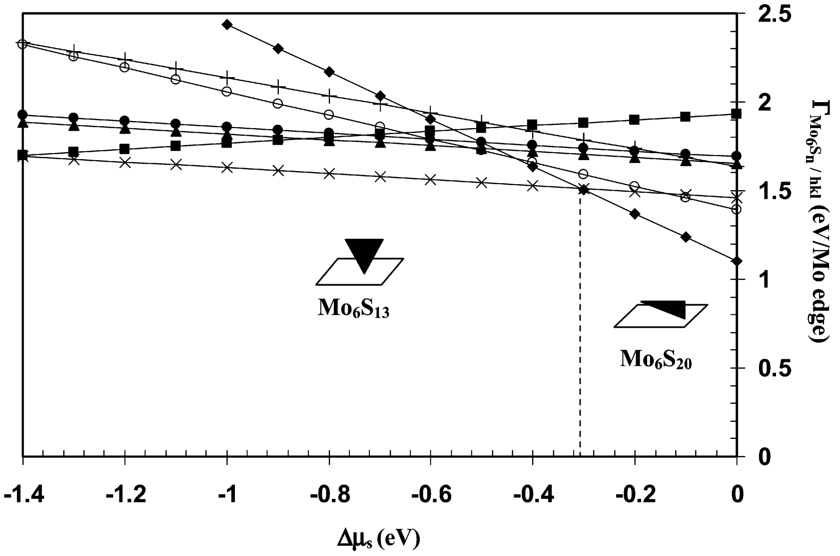

Fig. 10. Gibbs free energy diagram of the $Mo_6S_n$ clusters adsorbed on the anatase (001) surface. (◆) $Mo_6S_{20}$ (100% S, ∥); (○) $Mo_6S_{16}$ (100% S, 3c, e, ∥ or ⊥); (+) $Mo_6S_{15}$, (50% S, 3c, ∥); (▲) $Mo_6S_{13}$ (50% S, 5c, ∥); (●) $Mo_6S_{13}$ (50% S, 5c, tilted); (×) $Mo_6S_{13}$ (50% S, 5c, ⊥); (■) $Mo_6S_{11}$ (0% S, 5c, ⊥).

Table 2

Adhesion energies (in eV cluster) of the Co-promoted clusters compared to the non promoted clusters for relevant configurations with chemical interactions (⊥ or tilted) between the M(S)-edge and the γ-$Al_2O_3$ or $TiO_2$ surfaces

| Edge | γ-Alumina | | Anatase-$TiO_2$ | |
|---|---|---|---|---|
| | $E_{adh/100}$ | $E_{adh/110}$ | $E_{adh/101}$ | $E_{adh/001}$ |
| Mo-edge | $CoMo_5S_{14}$<br>−0.81<br>$Mo_6S_{14}$ (⊥, corner)<br>−1.29 [23] | $CoMo_5S_{14}$ (Fig. 11a)<br>−0.91<br>$Mo_6S_{14}$ (⊥, corner)<br>−1.60 [23] | $CoMo_5S_{13}$ (Fig. 11c)<br>−1.31<br>$Mo_6S_{13}$ (tilted)<br>−2.15 [23] | $CoMo_5S_{13}$ (Fig. 11d)<br>−1.5<br>$Mo_6S_{13}$ (tilted)<br>−1.89 [23] |
| S-edge | n.c. | $CoMo_5S_{13}$ (Fig. 11b)<br>−0.98<br>$Mo_6S_{13}$ (Fig. 5b)<br>−1.27 | $CoMo_5S_{15}$ (Fig. 11e)<br>−0.75<br>$Mo_6S_{15}$ (Fig. 7b)<br>−0.37 | $CoMo_5S_{16}$<br>−0.86<br>$Mo_6S_{16}$<br>−1.19 |

Table 3

Edge length, $k_T$ (in Mo atoms/edge), corresponding to the transition between chemical anchoring and parallel configuration under HDS conditions

| Surface | γ-$Al_2O_3$ | | | | Anatase-$TiO_2$ | | | |
|---|---|---|---|---|---|---|---|---|
| | (100) | | (110) | | (101) | | (001) | |
| | $k < k_T$ | $k_T$ | $k < k_T$ | $k_T$ | $k < k_T$ | $k_T$ | $k < k_T$ | $k_T$ |
| Mo-edge |  | 5 |  | 5 | 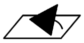 | 14 | 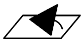 | 14 |
| S-edge | 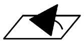 | 5 | 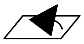 | 5 |  | 5 |  | 5 |

ues of $k_T$ for the two other support surfaces at a chemical potential close to HDS conditions ($\Delta\mu_S = -0.9$ eV). Similar conclusions can be drawn. Thus, only particles with very small $MoS_2$ clusters (certainly beyond the limits of current characterization techniques) are expected to be chemically anchored on γ-alumina. These results highlight the distinct behavior between anatase-$TiO_2$ and γ-alumina, and are discussed further in Section 4.

For the promoted CoMoS systems, the DFT results of adhesion energies obtained in Section 3.4 imply that for γ-alumina, Co does not stabilize particles with larger diameters in a perpendicular or tilted orientation. Only corners of very small particles of CoMoS may interact strongly with γ-alumina surfaces. On anatase-$TiO_2$, the strong adhesion energy of the nonpromoted Mo-edge implies that the stable CoMoS particles are anchored via the Mo-edge (without promoter atoms at the interface) for diameters as large as in the promoted case.

### *3.6. Morphology and edge wetting of supported $MoS_2$ and CoMoS particles*

Considering the data obtained on the S-edge and Mo-edge particles interacting with the supports, we are now able to determine the shape of the $MoS_2$ nanoparticles anchored on

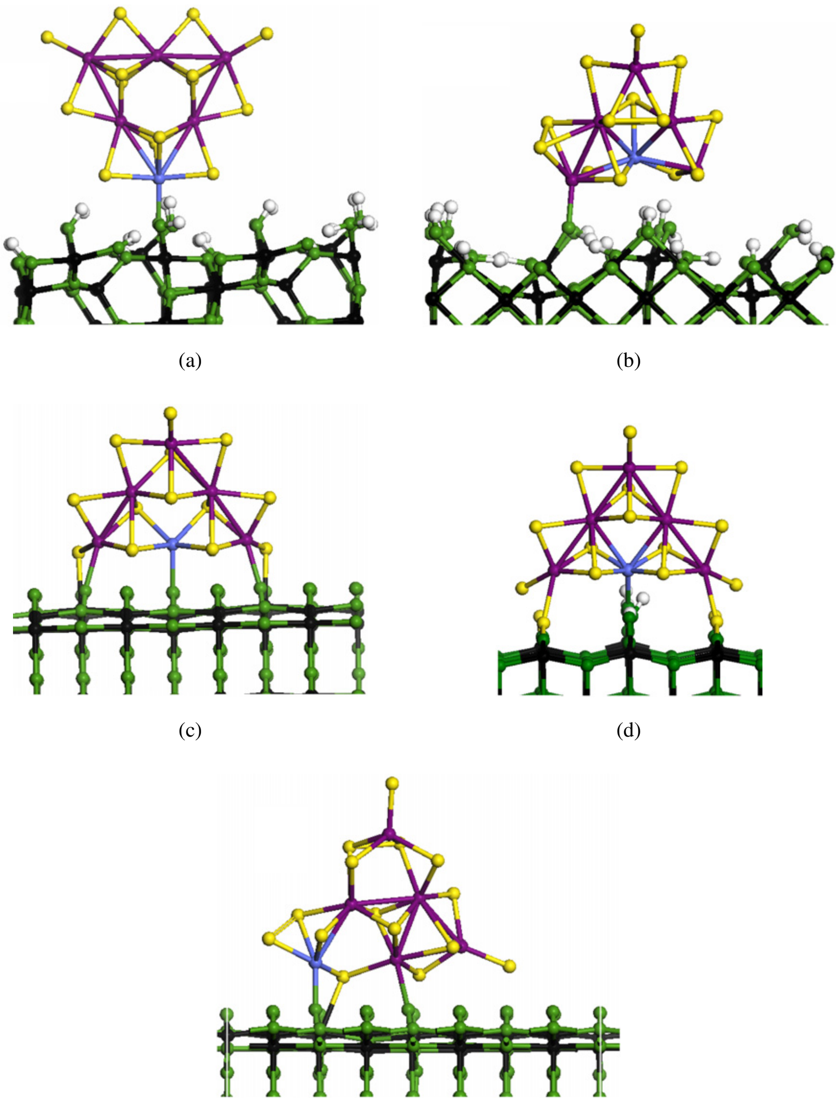
(a) (b)

(c) (d)

(e)

Fig. 11. Optimized structures of (a) $CoMo_5S_{14}$ of Mo-edge type and Co at the corner on $\gamma$-$Al_2O_3$ (110); (b) $CoMo_5S_{13}$ of S-edge type with Co at the edge on $\gamma$-$Al_2O_3$ (110); (c) $CoMo_5S_{13}$ of Mo-edge type with Co at the edge on $TiO_2$ (101); (d) $CoMo_5S_{13}$ of Mo-edge type with Co at the edge on $TiO_2$ (001); (e) $CoMo_5S_{15}$ of S-edge type with Co at the corner on $TiO_2$ (101). For the titania slab: black balls, aluminum atoms; green balls, oxygen; white balls, hydrogen atoms. For the $Mo_6S_n$ clusters: violet balls, molybdenum atoms; yellow balls, sulfur atoms. Blue balls, Co atoms. (For interpretation of the references to color in this figure legend, the reader is referred to the web version of this article.)

alumina or anatase at the thermodynamic equilibrium using the Gibbs–Curie–Wulff–Kaischew (GCWK) approach [37,38]. This approach is commonly used for supported metallic particles [39].

It was found that under HDS conditions, the unsupported (isolated) particles have a deformed hexagonal shape exposing more Mo-edge than S-edge, due to the lower surface energy of the Mo-edge [27,40]. We expect that, depending on the interaction with the support, the equilibrium morphology may change. Thus, in what follows we consider deformed hexagonal particles with surface free energies of the non-anchored S-edge, non-anchored Mo-edge and anchored Mo-edge.

Fig. 13a depicts the GCWK morphology of a particle anchored through the Mo-edge; the approach described herein can be easily extended to S-edge anchoring. Using the schematic configuration and notations of Fig. 13, the geometric parameters of the anchored particle's morphology can be deduced from the GCWK equations,

$$\frac{h_{\mathrm{Mo}}}{\Gamma_{\mathrm{Mo}}} = \frac{h_{\mathrm{S}}}{\Gamma_{\mathrm{S}}} = \frac{h_{\mathrm{Mo}}^{\mathrm{anch}}}{\Gamma_{\mathrm{Mo}}^{\mathrm{anch}}}, \tag{5}$$

where $h$ represents the distance of the particle center of gravity to the corresponding edges, $\Gamma_{\mathrm{Mo}}$ and $\Gamma_{\mathrm{S}}$ are the surface energies of the free edges, and $\Gamma_{\mathrm{Mo}}^{\mathrm{anch}}$ is the surface energy of the anchored Mo-edge. According to this definition, $h_{\mathrm{Mo}}^{\mathrm{anch}}$ and $\Gamma_{\mathrm{Mo}}^{\mathrm{anch}}$ are algebraic values and are allowed to become negative, because $h_{\mathrm{Mo}}^{\mathrm{anch}}$ is the center's height or depth of the virtual noninteracting particle. As explained previously, $\Gamma_{\mathrm{Mo}}^{\mathrm{anch}}$ depends on the adhesion energies (negative by convention if anchor-

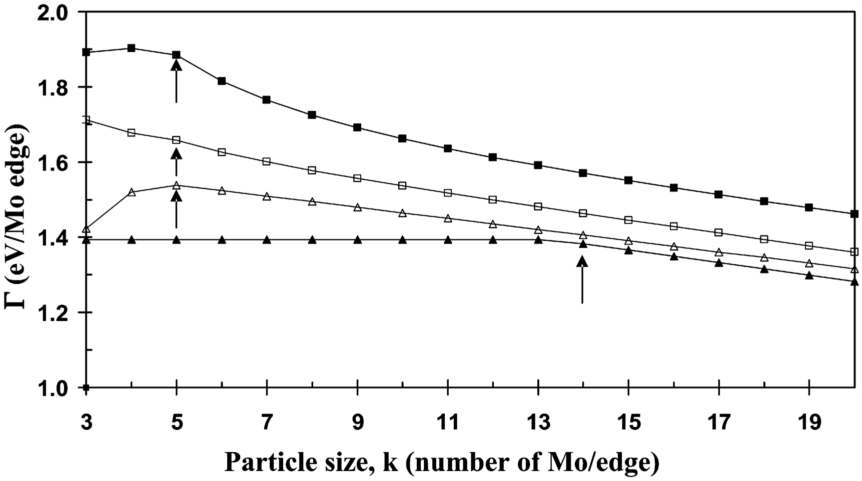

Fig. 12. Gibbs free energy of the supported $MoS_2$ particles as a function of size represented by $k$ (number of Mo per edge) on the anatase-$TiO_2$ (101) surface (plain symbols) surface and the $\gamma$-alumina (110) surface (empty symbols) at $\Delta\mu_S = -0.9$ eV (HDS conditions). (△, ▲) Mo-edge; (□, ■) S-edge. Arrows indicate the threshold $k_T$ values for the edge anchored/parallel orientation transition.

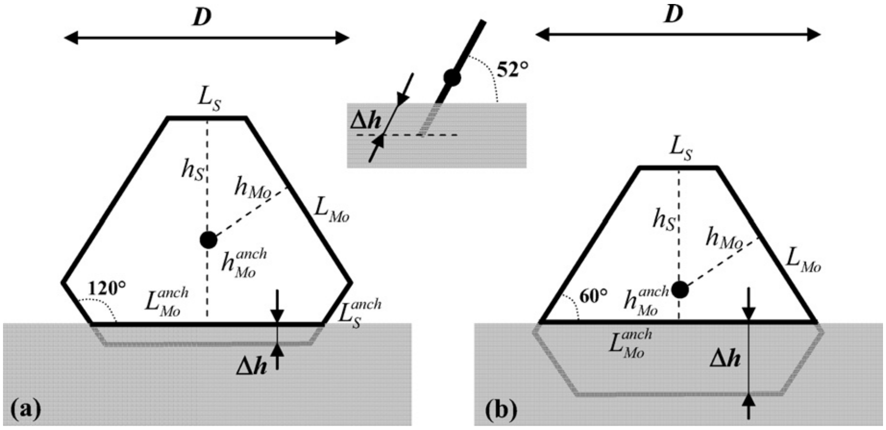

Fig. 13. Schematic Gibbs–Curie–Wulff morphologies for the supported $MoS_2$ particles anchored by the Mo-edge on the $TiO_2$ (101) surface (a) case for $L_S^{anch} > 0$; (b) stable configuration in HDS conditions ($\Delta\mu_S = -0.9$ eV) and $L_S^{anch} = 0$. The plane of the $MoS_2$ monolayer is tilted with respect to the normal of the surface (see insets and [23]).

ing through the Mo-edge exists) and the chemical potential of S,

$$\Gamma_{Mo}^{anch}(\Delta\mu_S) = \Gamma_{Mo}(\Delta\mu_S) + E_{adh}. \tag{6}$$

From Eqs. (5) and (6), it follows that

$$\frac{\Delta h}{h_{Mo}} = \frac{-E_{adh}}{\Gamma_{Mo}} = 1 - \beta, \tag{7}$$

where $\beta = \Gamma_{Mo}^{anch}/\Gamma_{Mo}$ (according to the value of $E_{adh}$, $\beta = 0.19$). In the same spirit as for metallic particles [39], different edge-wetting regimes of the supported $MoS_2$ particles can be defined as a function of the $\Delta h/h_{Mo}$ ratio:

- For $\beta \geqslant 1$, there is no edge wetting by the Mo-edge; the particle lies parallel to the surface. This can be defined as basal wetting of the support by the particles.
- For $0 < \beta < 1$, the edge wetting by the Mo-edge is bad.
- For $-1 < \beta \leqslant 0$, the edge wetting by the Mo-edge is good.
- For $\beta \leqslant -1$, the edge wetting is perfect.

The relevant geometric parameters for the morphology depend on the respective values of $\beta$ and $\alpha = \Gamma_S/\Gamma_{Mo}$. When the particle exposes both edges ($1/2 < \alpha < 2$) and for $\alpha - 1 < \beta < 1$ (i.e., $\Gamma_S < 2\Gamma_{Mo} + E_{adh}$), $L_{Mo}^{anch}$ remains $> 0$, as represented by the configuration of Fig. 13a,

$$\frac{L_{Mo}^{anch}}{L_{Mo}} = \frac{2\alpha - \beta}{2\alpha - 1}, \tag{8}$$

$$\frac{L_S^{anch}}{L_S} = \frac{1 - \alpha + \beta}{2 - \alpha}, \tag{9}$$

$$\frac{L_S}{L_{Mo}} = \frac{2 - \alpha}{2\alpha - 1}. \tag{10}$$

For $\beta \leqslant \alpha - 1$ (i.e., $\Gamma_S \geqslant 2\Gamma_{Mo} + E_{adh}$), $L_S^{anch}$ is equal to 0, as represented by the configuration in Fig. 13b, and the other geometric parameters are

$$\frac{L_{Mo}^{anch}}{L_{Mo}} = \frac{2 + \beta}{\alpha + \beta} \tag{11}$$

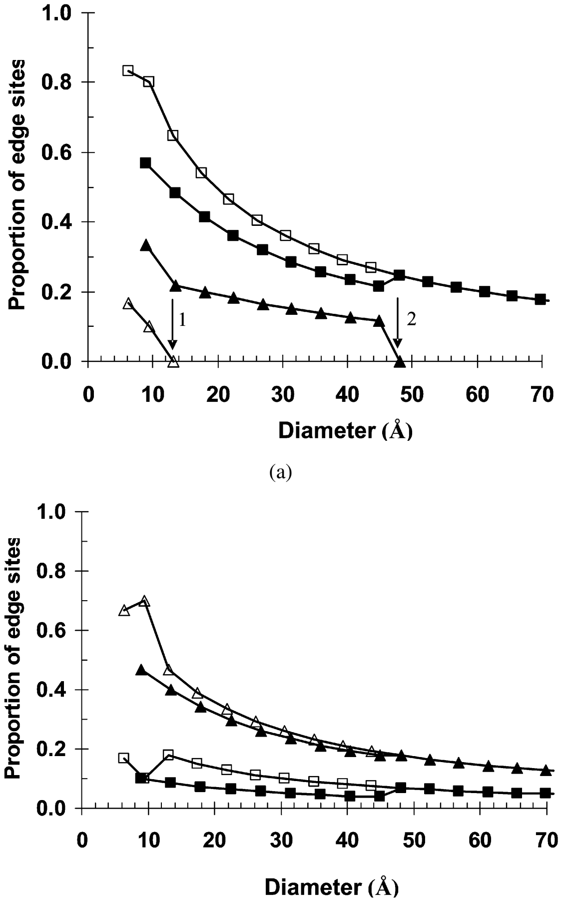

(a)

(b)

Fig. 14. (a) Proportion of non-anchored (free) and anchored Mo-edge sites (respective to the total number of Mo atoms) as a function of the $MoS_2$ particles diameter (as defined in Fig. 13). (△) Mo-edge atoms anchored on $\gamma$-alumina ($L_{Mo}^{anch}$); (☐) free Mo sites at S- and Mo-edge on $\gamma$-alumina; (▲) Mo-edge atoms anchored on anatase; (■) free Mo sites at the S- and Mo-edge on anatase. (Arrows represent the transition between edge-anchored (edge-wetting) particles and flat lying particles.) (b) Distribution of free edge sites: (△) Mo-edge sites on $\gamma$-alumina; (☐) S-edge sites on $\gamma$-alumina; (▲) Mo-edge sites on anatase; (■) S-edge sites on anatase.

and

$$\frac{L_S}{L_{Mo}} = \frac{2-\alpha}{\alpha+\beta}. \tag{12}$$

Note that the definition of the edge-wetting regime depends neither on $\alpha$ nor on the existence of $L_S^{anch}$. Considering these morphologies and using geometric models analogous to [41] for anchored and nonanchored particles, the proportion of edge sites (anchored, nonanchored, S-edge, and Mo-edge) is deduced as a function of particles diameter and reported in Figs. 14 and 15.

### 3.6.1. Nonpromoted particles

Table 4 reports the numerical values of the geometrical parameters for a given particle size stable in such an anchoring mode on anatase ($k_T < 14$) under HDS conditions. In particular, the Gibbs free energy values under HDS conditions for the nonanchored edges were calculated for large stable edges in [27] ($\Gamma_{Mo} = 1.19$ eV/surface unit and $\Gamma_S =$ 1.61 eV/surface unit), leading to $\alpha = 1.35$. The value used for is taken from our previous work [23] for the case of Mo-edge anchoring. On the (101) anatase $TiO_2$ surface, the stable configuration was the tilted $Mo_6S_{14}$ or $Mo_6S_{13}$ clusters, with adhesion energies of −1.60 or −1.66 eV per cluster. Adding van der Waals contributions (−0.08 eV per S atom) estimated previously [23] led to $E_{adh}$ equal to −0.96 or −0.99 eV per Mo atom belonging to the anchored edge.

Thus, the two S-edges located on each side of the anchored Mo-edge are no longer present ($L_S^{anch} = 0$). As shown in Fig. 13b, the anchored Mo-edge, $L_{Mo}^{anch}$, is longer than the noninteracting one, $L_{Mo}$. Furthermore, a $\Delta h/h_{Mo}$ ratio <1 characterizes the bad "edge-wetting regime" of the sulfide particles even if $L_S^{anch} = 0$. The morphology of anatase-supported $MoS_2$ particles can be defined as trapezoidal.

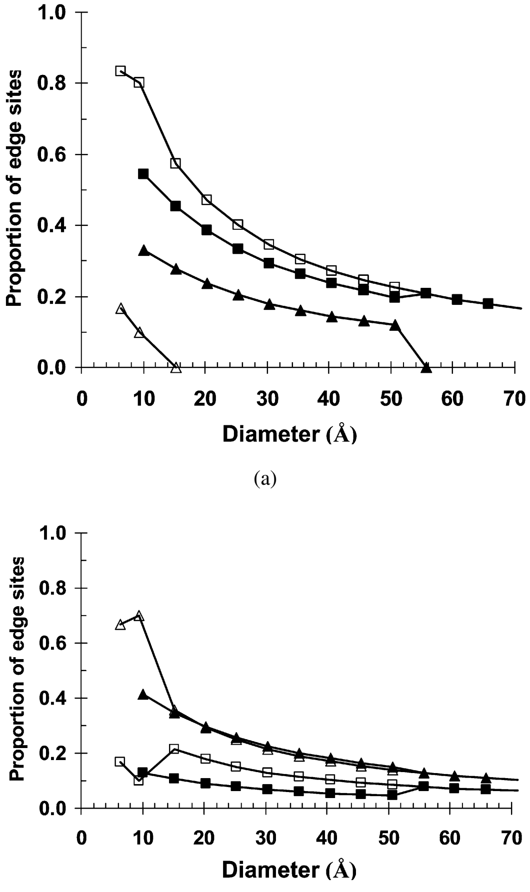

(a)

(b)

Fig. 15. Distribution of edge sites for the promoted CoMoS particles supported on $\gamma$-alumina and anatase. Same legend as in Fig. 14.

Table 4
Morphology parameters of the $MoS_2$ particles anchored through the Mo-edge on the $TiO_2$ (101) surface under HDS conditions (i.e., particle with $k_T < 15$). The notations are defined in Fig. 13b

| Active phase | $\alpha$ | $\beta$ | $\Delta h/h_{Mo}$ | $L_S/L_{Mo}$ | $L_{Mo}^{anch}/L_{Mo}$ | $L_S^{anch}/L_S$ |
|---|---|---|---|---|---|---|
| $MoS_2$ | 1.35 | 0.19 | 0.61 | 0.42 | 1.42 | 0 |
| CoMoS | 1.18 | 0.19 | 0.61 | 0.60 | 1.60 | 0.01 |

For the $\gamma$-alumina surfaces, the edge wetting by the sulfide particles is even weaker due to the low adhesion energy reported in this paper or in previous work [23] characterizing the weaker ligand effect of this support.

According to this morphology, we can evaluate the proportion of free and anchored Mo-edge atoms (with respect to the total of Mo atoms). Fig. 14a shows these distributions as a function of particle diameter for the $\gamma$-alumina (110) and the anatase (101) surfaces. Similar results, not reported here, were obtained for the other two surfaces. As shown, the transition between chemically anchored (edge wetting) and "flat lying" (basal wetting) particles occurs for smaller sizes on $\gamma$-alumina than on anatase: $D = 15$ Å (arrow 1) versus $D = 45$ Å (arrow 2). Consequently, for the same particle size (<45 Å), $MoS_2$ on alumina exhibits a proportion of free Mo-edge atoms (empty squares in Fig. 14a) 1.3 higher than that on anatase (plain squares) due to the loss of anchored Mo-edge atoms (plain triangles) involved in the wetting of the anatase surface. However, the TEM particle sizes are not the same on the two supports. This effect is discussed in Section 4. Fig. 14b shows the distributions of the S-edge and Mo-edge sites on the two supports. It appears that the proportion and variation of Mo-edge sites are rather similar, whereas S-edge sites are significantly more numerous on $\gamma$-alumina for diameters <45 Å. The consequences of these results with respect to TEM and catalytic activity data are further detailed in Section 4.

### 3.6.2. Case of promoted CoMoS particles

According to the work by Schweiger et al. [16], the surface energies for the Co-promoted S-edge and nonpromoted Mo-edge lead to a value of $\alpha$ of about 1.18. According to Section 3.4, the particles are anchored through the nonpromoted Mo-edge, the value of $\beta$ thus remains unchanged. The morphological parameters reported in Table 4 show that the decrease in $\alpha$ implies an enhanced S-edge. The value of $L_S^{\text{anch}}$ is not rigorously equal to 0, even if very close to 0. Consequently, adding the promoter mainly influences the proportion of the S-edge sites, as shown in Fig. 15b. As for the nonpromoted case, the consequences of these results with respect to TEM and catalytic activity data are further detailed in Section 4.

## 4. Discussion

The preceding results provide new insight into sulfide active phase–support interactions. They enrich our previous work [23] and allow a rather exhaustive comparison with experimental results available in the literature.

For nonpromoted $MoS_2$ supported either on $\gamma$-alumina or on anatase-$TiO_2$, the present investigation implies that the S-edge does not interact strongly with the four relevant support surfaces. As proposed previously [23], the ligand effect of $\gamma$-alumina remains weak whatever the interacting edge considered for the $MoS_2$ active phase. On anatase-$TiO_2$, a distinction between the Mo-edge and the S-edge is clearly identified. Indeed, the epitaxial relationship exists only between the anatase surfaces and the Mo-edge. According to our simulations, no such epitaxial relationship is possible between the S-edge and the surface due to the mismatch between the Mo-, S-, Ti-, and O-atomic networks at the interface, which does not enable the formation of Mo–S(O)–Ti–O–Mo rings as found for the Mo-edge. Consequently, the strong chemical ligand effect of anatase-$TiO_2$ is oriented toward the Mo-edge of the $MoS_2$ active phase. This finding seems to contradict recent theoretical studies by Hinnemann et al. [29] suggesting that the S-edge would be the one at the support–active phase interface. To explain this discrepancy, recall that Hinnemann et al. [29] proposed mimicking the interaction with the support by exchanging S atoms at the $MoS_2$ edges with –OH groups produced from water molecules. But this approach does not take into account the local geometric constraints and electronic properties of the Lewis and Brønsted active sites of the support. Our results demonstrate that the complex nature of sites present on the support may change the interface stability, and thus considering the exact nature of the support surface is crucial.

Regarding size effects, we have found that on the $\gamma$-alumina surface, a chemical interaction involving the formation of Mo–O–Al bonds is possible only at the corner of very small particles (edge length <10 Å), probably not visible by electronic microscopy. The resulting orientation of the $MoS_2$ particles with usual sizes should be with the basal plane parallel to the support surface. On anatase-$TiO_2$, insights resulting from this paper and previous work [23] show that large $MoS_2$ particles can be anchored through Mo–O(S)–Ti bonds in a tilted orientation. One Mo-edge is located at the interface with the support for edge length <45 Å ($k < 15$).

Numerous attempts to identify the mode of the $MoS_2/\gamma$-alumina interaction by use of electron microscopy have been reported in the literature. Earlier studies, reviewed by Luck [42], reported that the $MoS_2$ slabs may be oriented normally or parallel to the support surface. Vrinat et al. [43] concluded that the basal planes of $MoS_2$ crystallites lie parallel to the alumina surface, a result also found by others [44,45]. Pratt et al. [46] recommended using HREM at the location of $MoS_2$ vertically to the surface of the support. More recent studies by Sakashita et al. [47,48] favored basal adsorption of single $MoS_2$ sheet on the (110) surface and edge anchoring for $MoS_2$ on the (100) surface. Even more recently, Shimada suggested that only small size particles are edge-bonded, because of the large lattice misfit between $MoS_2$ and $\gamma$-$Al_2O_3$ (100) [7]. The same author reported sizes of 30–50 Å for basal-bonded single $MoS_2$ layers on the (110) surface and stacked $MoS_2$ sheets on the (111) and (100) surfaces. Our present theoretical results seem to be in line with the latter characterization and suggest that most $MoS_2$ single layers are thermodynamically stable when the basal plane lies parallel to the $\gamma$-alumina surfaces. Edge- or corner-bonded layers are restricted to very small $MoS_2$ clusters. The very poor edge wetting of alumina by sulfide particles is the possible explanation for these observations.

On the anatase support, within the limit of the techniques used, experimental work seems to put forward the presence of edge-bonded $MoS_2$ particles with chemical Mo–O–Ti bridges. On one hand, EXAFS studies by Leliveld et al. [24] reveal a higher Mo–O coordination number on anatase than on $\gamma$-alumina. On the other hand, tilted orientation of $MoS_2$ layers on anatase have been observed by HRTEM [49,50]. Our theoretical results are in line with such experimental observations and indicate that, in addition, edge bonding occurs through the Mo-edge of the $MoS_2$ particles.

We also provide a new prediction of the shape of edge-bonded $MoS_2$ particles on anatase-$TiO_2$ (Fig. 13). To the best of our knowledge, no characterization technique has been able to furnish such subtle morphology characterization on oxide supports. Our density functional theory calculation results show that the "wetting regime" of edge-anchored particles is weak on $\gamma$-alumina and significantly improved on anatase-$TiO_2$, with crucial consequences for the number and nature of sites, as discussed in what follows.

The average $MoS_2$ particle sizes calculated from histogram diagrams reported previously [5] is ca. 38 Å for the titania support and ca. 49 Å for $\gamma$-alumina. For $MoS_2$ supported on mixed-phase $TiO_2$–$Al_2O_3$, a similar trend is observed: decreasing average crystallite length in mixtures with a decreasing $TiO_2/(TiO_2 + Al_2O_3)$ ratio [51]. Even if according to TEM accuracy there is a slight overestimation of average sizes on both supports, our following arguments will not change. First, the Mo-edge wetting by anatase is at the origin of the smaller particle sizes observed on anatase. Then, using these two diameter values in the diagrams of Fig. 14a leads to a similar proportion of free edge sites (including nonanchored Mo and S edges) on anatase-$TiO_2$ (25–30%) and $\gamma$-alumina (24–29%). Thus, the number of Mo edge atoms trapped at the $MoS_2$/anatase interface is compensated for by the smaller sizes of edge-anchored particles and the decrease of Mo bulk atoms. The calculated proportion of free edge sites cannot explain the activity factor of 4.4 (expressed by Mo atom) observed on anatase. Consequently, the main part of the higher activity observed on anatase must be found in intrinsic effects on the nature of sites. According to Fig. 14b, the relative distribution of S-edge and Mo-edge sites is 21% on anatase and 38% on $\gamma$-alumina for the two sizes. The loss of two S-edges on anatase is induced by the edge wetting of anatase. Furthermore, Arrouvel et al. [23] found that the ligand effect of anatase on anchored $MoS_2$ clusters exposing Mo-edge only stabilizes sulfur-deficient particles exhibiting more vacancies required for the HDS reaction. These two combined effects certainly elucidate the enhancement of the intrinsic activity on anatase-$TiO_2$ as observed previously for nonpromoted particles [5].

At this stage, it is difficult to quantitatively evaluate whether the tilted orientation of $MoS_2$ particles on anatase may play a positive or negative role for site accessibility and steric hindrance. Knowing that the nature and bulkiness of the reactant also should be considered, such considerations are beyond the scope of the current work.

Regarding the promoted CoMoS phase, its interaction with alumina is reduced to single-point anchoring, probably involving one Mo atom, because the interaction through the Co atom is not energetically favored (see Table 2). One exception to this general trend has to be found in corner interaction for which Co atom might be more favourable; however, this local effect concerns very small corner-bonded particles. Thus, this result is in agreement with Mössbauer studies showing that the support interactions involve the Mo atoms and not the promoter atoms [52,53].

On $\gamma$-alumina, Ramirez et al. [5] observed by TEM that the addition of Co implies a displacement of particle size distribution toward smaller diameters with respect to nonpromoted ones [5]. Nonpromoted particles exhibit a mean size of 49 Å; promoted CoMoS particles, ca. 40 Å. The ligand effect of the Co promoter enables decreasing the edge energy of the particles [16], which stabilizes particles with higher edge-to-volume ratios. In summary, the increased activity under HDS observed on $\gamma$-alumina is due essentially to the electronic effect of the promoter [14,15,17] and the decreased particle size.

On anatase-$TiO_2$, two effects are revealed by the present DFT work for promoted systems. A strong Mo-edge/support interaction exists for the nonpromoted systems. TEM analysis shows that the Co promotion also modifies the size distribution now centered around 30 Å [5].

According to Fig. 15a, the proportion of free edge sites (including nonanchored Mo- and S-edges), is about 29–38% on anatase and 27–31% on $\gamma$-alumina (within the accuracy assumed for the estimation of mean sizes by TEM). As for the nonpromoted case, the total number of free sites for CoMoS remains similar on anatase and $\gamma$-alumina. Thus, dispersion effects can be ruled out to explain different activities. The promoting effect on anatase (factor of 1.7) is significantly less pronounced than that on $\gamma$-alumina (factor of 7.6) [5]. According to Fig. 15b, the S-edge sites are about 23% more prevalent than Mo-edge sites on anatase and 60% more prevalent on $\gamma$-alumina. Previous DFT studies [16] found that Co preferentially locates on the S-edge. Thus, the loss of S-edge sites on anatase impairs optimal promoter distribution in decoration of the supported CoMoS particles. The different nature of promoted sites on $\gamma$-alumina and anatase induced by different edge-wetting regimes also elucidates the origin of the different intrinsic activities of CoMoS particles on the two supports.

## 5. Conclusion

DFT molecular modeling of $MoS_2$ and CoMoS supported on $\gamma$-alumina and anatase $TiO_2$ was used for rationalizing the phase–support interaction and its role on HDS activity. The following conclusions are fully consistent with the earlier proposals by Ramirez et al. [5] that "catalyst activities calculated on the basis of edge surface area from the HREM results also show that the $TiO_2$-supported catalysts are more active than $Al_2O_3$-supported catalysts. We suggest that the role of $TiO_2$ is to promote the formation of edge-up $MoS_2$ particles due to an interaction between the $MoS_2$ edge planes and some planes of $TiO_2$. These particles are intrinsically more active than the randomly distributed $MoS_2$ particles found in $Al_2O_3$."

Based on the edge-wetting concept, our quantitative DFT insights give a rational interpretation of the intrinsic catalytic behavior of $MoS_2$ and CoMoS supported on anatase and $\gamma$-alumina.

For the nonpromoted $MoS_2$ active phase, the following conclusions can be stated:

- On $\gamma$-$Al_2O_3$ (110) and (100) surfaces, $MoS_2$ particles of very small size (<15 Å) exhibit chemical interaction as Mo–O–Al bonds for both Mo- and S-edges. For commonly seen sizes (>15 Å), H bonds and van der Waals interactions stabilize the particles in a parallel orientation to the surface.
- On anatase-$TiO_2$ (101) and (001) surfaces, an epitaxial relationship is formed between the Mo-edge of $MoS_2$ particles and the support surfaces, with the formation of Mo–O–Ti–S–Mo rings. This epitaxy is not possible between the S-edge and the $TiO_2$ surface. Particles with sizes up to 45 Å are strongly anchored at the surface through the Mo-edge. This trend was previously termed the "chemical ligand effect" of anatase-$TiO_2$ [23].
- The edge-wetting regime of the $MoS_2$ particles is weak for $\gamma$-$Al_2O_3$, and the morphology of the isolated particles is modified only slightly by the support's effect. In anatase-$TiO_2$, the wetting is significantly increased and the anchored $MoS_2$ particles exhibits a trapezoidal morphology with two predominant Mo-edges and one single S-edge.
- The smaller particles size observed by TEM on anatase-$TiO_2$ is attributed to the stronger edge wetting of the support by $MoS_2$ particles. However, rigorous free edge site counting have shown that size or dispersion effects cannot account for the different activities observed on anatase and $\gamma$-alumina.
- The higher HDS activity observed on anatase-$TiO_2$-supported $MoS_2$ is attributed to the edge-wetting and ligand effects of anatase. The different natures of edge sites (higher Mo-edge/S-edge on anatase) and the stabilization of sulfur-deficient particles induced by the strong ligand effect of anatase are at the origin of the higher HDS activity observed on anatase.

For the promoted CoMoS active phase, the following findings are noted:

- Promotion by Co generally weakens the edge interaction between the support $TiO_2$ and $\gamma$-$Al_2O_3$. Corner effects may invert this trend on $TiO_2$; however, they remain limited to very small particle sizes.
- On $\gamma$-$Al_2O_3$, the ligand effect of the promoter (i.e., decoration of the $MoS_2$ particles by the promoter) is predominant. Smaller particles sizes on $\gamma$-alumina are stabilized by the ligand effect of the promoter, which diminishes the Mo- and S-edge energies.
- As for the nonpromoted active phase, the enumeration of free edge sites on anatase and $\gamma$-alumina shows that dispersion effects cannot explain the different promotion effects on HDS activities.
- The different HDS catalytic activities for the promoted systems on the two supports are explained by the distinct edge-wetting regimes inducing a significant higher S-edge/Mo-edge ratio on $\gamma$-alumina, which is favorable for optimal promoter decoration.

The edge wetting of the support by $MoS_2$ and CoMoS appears to be a key factor in understanding the effect of supports in catalysis by sulfides. A possible area for future exploration is whether this concept can be extended to other types of supports as the two investigated herein (e.g., zirconia, ceria). Finally, DFT results [16] have revealed that promoter Ni has a stronger affinity for the Mo-edge than Co. Specific catalytic behavior recently observed for anatase- and zirconia-supported NiMoS [54] could be explored in light of the edge-wetting concept.

## Acknowledgments

Part of this work was undertaken within the Groupement de Recherche Européen "Dynamique Moléculaire Quantique Appliquée à la Catalyse," a joint IFP-CNRS-TOTAL-Universität Wien project. The authors thank Professor Steve Parker for a careful reading of the paper. P.R. is indebted to Denis Guillaume from IFP for fruitful discussions. The referees are acknowledged for their interesting suggestions.

## Supplementary materials

The online version of this article contains additional supplementary material.

Please visit doi: 10.1016/j.jcat.2006.12.007.

## References

[1] H. Topsøe, B.S. Clausen, F.E. Massoth, in: J.R. Anderson, M. Boudart (Eds.), Hydrotreating Catalysis—Science and Technology, vol. 11, Springer-Verlag, Berlin/Heidelberg, 1996.
[2] R. Prins, in: G. Ertl, H. Knözinger, J. Weitkamp (Eds.), Handbook of Heterogeneous Catalysis, vol. 4, Wiley–VCH, Weinheim, 1997, p. 1908.
[3] M. Breysse, J.L. Portefaix, M. Vrinat, Catal. Today 10 (1991) 489.
[4] M. Breysse, P. Afanasiev, C. Geantet, M. Vrinat, Catal. Today 86 (2003) 5.
[5] J. Ramirez, S. Fuentes, G. Díaz, M. Vrinat, M. Breysse, M. Lacroix, Appl. Catal. 52 (1989) 211.
[6] W. Qian, H. Zhang, Y. Okoshi, A. Ishihara, T. Kabe, J. Chem. Soc. Faraday Trans. 9 (1997) 1821.
[7] H. Shimada, Catal. Today 86 (2003) 17.
[8] J. Ramirez, L. Cedeno, G. Busca, J. Catal. 184 (1999) 59.
[9] L. Coulier, J.A.R. van Veen, J.W. Niemantsverdriet, Catal. Lett. 79 (2002) 149.
[10] D. Wang, W. Qian, A. Ishihara, T. Kabe, Appl. Catal. A Gen. 224 (2002) 191.
[11] G. Muralhidar, F.E. Massoth, J. Shabtai, J. Catal. 85 (1984) 44.
[12] D. Wang, X. Li, E.W. Qian, A. Ishihara, T. Kabe, Appl. Catal. A Gen. 238 (2003) 109.
[13] P. Raybaud, Appl. Catal. A Gen. (2007), doi:10.1016/j.apcata.2007.01.005.
[14] P. Raybaud, J. Hafner, G. Kresse, S. Kasztelan, H. Toulhoat, J. Catal. 190 (2000) 128.
[15] L.S. Byskov, B. Hammer, J.K. Norskov, B.S. Clausen, H. Topsoe, Catal. Lett. 47 (1997) 177.
[16] H. Schweiger, P. Raybaud, H. Toulhoat, J. Catal. 212 (2002) 33.
[17] A. Travert, H. Nakamura, R.A. van Santen, S. Cristol, J.F. Paul, E. Payen, J. Am. Chem. Soc. 124 (2002) 7084.
[18] M. Digne, P. Sautet, P. Raybaud, P. Euzen, H. Toulhoat, J. Catal. 211 (2002) 1.
[19] M. Digne, P. Sautet, P. Raybaud, P. Euzen, H. Toulhoat, J. Catal. 226 (2004) 54.

[20] M. Digne, P. Raybaud, P. Sautet, H. Toulhoat, L'Actualité Chimique 298 (2006) 23.
[21] C. Arrouvel, H. Toulhoat, M. Breysse, P. Raybaud, J. Catal. 226 (2004) 260.
[22] C. Arrouvel, M. Digne, M. Breysse, H. Toulhoat, P. Raybaud, J. Catal. 222 (2004) 152.
[23] C. Arrouvel, M. Breysse, H. Toulhoat, P. Raybaud, J. Catal. 232 (2005) 161.
[24] R.G. Leliveld, A.J. van Dillen, J.W. Geus, D.C. Koningsberger, J. Catal. 165 (1997) 184.
[25] X. Krokidis, P. Raybaud, A.-E. Gobichon, B. Rebours, P. Euzen, H. Toulhoat, J. Phys. Chem. B 105 (2001) 5121.
[26] S. Dzwigaj, C. Arrouvel, M. Breysse, C. Geantet, S. Inoue, H. Toulhoat, P. Raybaud, J. Catal. 236 (2005) 245.
[27] H. Schweiger, P. Raybaud, G. Kresse, H. Toulhoat, J. Catal. 207 (2002) 76.
[28] S. Helveg, J.V. Lauritsen, E. Lægsgaard, I. Stensgaard, J.K. Nørskov, B.S. Clausen, H. Topsøe, F. Besenbacher, Phys. Rev. Lett. 84 (2000) 951.
[29] B. Hinnemann, J.K. Norskov, H. Topsøe, J. Phys. Chem. B 109 (2005) 2245.
[30] J.P. Perdew, Y. Wang, Phys. Rev. B 45 (1992) 13244.
[31] G. Kresse, J. Furthmüller, Comput. Mater. Sci. 6 (1996) 15.
[32] G. Kresse, D. Joubert, Phys. Rev. B 59 (1999) 1758.
[33] H. Rydberg, M. Dion, N. Jacobson, E. Schröder, P. Hyldgaard, S.I. Simak, D.C. Langreth, B.I. Lundqvist, Phys. Rev. Lett. 91 (2003) 126402.
[34] J.V. Lauritsen, M.V. Bollinger, E. Lægsgaard, K.W. Jacobsen, J.K. Nørskov, B.S. Clausen, H. Topsøe, F. Besenbacher, J. Catal. 221 (2004) 510.
[35] L.S. Byskov, J.K. Nørskov, B.S. Clausen, H. Topsøe, J. Catal. 187 (1999) 109.
[36] L.S. Byskov, J.K. Norskov, B.S. Clausen, H. Topsoe, Catal. Lett. 64 (2000) 95.
[37] M.P. Curie, Bull. Soc. Min. Fr. 8 (1885) 145.
[38] G. Wulff, Z. Kristallogr. 34 (1901) 449.
[39] C.R. Henry, Prog. Surf. Sci. 80 (2005) 92.
[40] J.V. Lauritsen, M. Nyberg, J.K. Nørskov, B.S. Clausen, H. Topsøe, E. Lægsgaard, F. Besenbacher, J. Catal. 224 (2004) 94.
[41] S. Kasztelan, H. Toulhoat, J. Grimblot, J.P. Bonnelle, Appl. Catal. 13 (1984) 127.
[42] F. Luck, Bull. Soc. Chim. Belg. 100 (1991) 781.
[43] M. Vrinat, D. Hamon, M. Breysse, B. Durand, T. des Courières, Catal. Today (1994) 273.
[44] S. Srinivasan, A.K. Datye, C.H.F. Peden, J. Catal. 137 (1992) 513.
[45] R.M. Stockmann, H.W. Zandbergen, A.D. van Langeveld, J.A. Moulijn, J. Mol. Catal. A Chem. 102 (1995) 147.
[46] K.C. Pratt, J.V. Sanders, V. Christov, J. Catal. 124 (1990) 416.
[47] Y. Sakashita, T. Yoneda, J. Catal. 185 (1999) 487.
[48] Y. Sakashita, Surf. Sci. 489 (2001) 45.
[49] Y. Sakashita, Y. Araki, K. Honna, H. Shimada, Appl. Catal. A Gen. 197 (2000) 247.
[50] Y. Sakashita, Y. Araki, H. Shimada, Appl. Catal. A Gen. 215 (2001) 101.
[51] J. Ramirez, L. Ruiz-Ramirez, L. Cedeno, V. Harle, M. Vrinat, M. Breysse, Appl. Catal. A Gen. 93 (1993) 163.
[52] H. Topsoe, R. Candia, N.-Y. Topsoe, B.S. Clausen, Bull. Soc. Chim. Belg. 93 (1984) 783.
[53] J.A.R. van Veen, E. Gerkema, A.M. Knoester, J. Chem. Soc. Chem. Commun. (1987) 1684.
[54] Y. Ji, P. Afanasiev, M. Vrinat, L. Wenzhao, L. Can, Appl. Catal. A Gen. 257 (2004) 157.